Alma Mater Studiorum - Università di Bologna

SCUOLA DI SCIENZE

Dipartimento di Chimica Industriale "Toso Montanari"

Corso di Laurea Magistrale in

Chimica Industriale

Classe LM-71 – Scienze e Tecnologie della Chimica Industriale

Computational and experimental investigations of the catalytic transfer hydrogenation of methyl levulinate with ethanol on ZrO_2

Tesi di laurea sperimentale

CANDIDATO

Lorenzo Mauro

RELATORE

Prof. Ivan Rivalta

CORRELATORE

Prof. Tommaso Tabanelli

Dr. Fabio Loprete

Dr. Luca Visentin

Anno Accademico 2023-2024

Abstract

The reduction of levulinic esters to γ-valerolactone is a key step in the valorization of biomass-derived compounds, providing sustainable pathways for producing various bio-based products. This thesis investigates the formation of angelica lactones (ALs), hypothesized as key intermediates in the catalytic transfer hydrogenation of methyl levulinate (ML) with ethanol in the gas phase over tetragonal zirconia (*t*-ZrO_2) catalyst. Both experimental and computational investigations are integrated to investigate this process.

The experimental studies involve Diffuse Reflectance Infrared Fourier Transform Spectroscopy (DRIFTS) to analyze surface species and the mechanism behind the transformation of ML into ALs. These findings are complemented by computational studies based on Periodic Density Functional Theory (DFT), providing fundamental insights into molecular adsorption modes, reaction intermediates structures, and spectroscopic properties (e.g. vibrational frequencies).

Experimentally, the behavior of ML and related compounds (such as methyl valerate and 2-pentanone) on the catalyst surface is examined across various temperatures. DRIFTS results reveal that ML forms levulinate-like species (bidentate intermediates) on the zirconia surface, even at room temperature, with more pronounced effects as the temperature rises. At the reaction temperature of 250 °C, the DRIFTS spectra of ML and angelica lactone (αAL) are nearly identical, indicating that either ML is converted into ALs or αAL is reverted to a common intermediate shared with ML, possibly a levulinate-like. On the computational side, DFT simulations model the adsorption of key molecules on the catalyst surface, revealing strong interactions between the ester group of ML and ALs with the *t*-ZrO_2 (101) facet, which results in significant molecular distortion, consistent with experimental findings. The simulations also revealed the role of surface hydroxyl groups in facilitating the cyclization of ML into αAL while preventing surface poisoning. Simulated vibrational spectra further helped interpreting the specific surface species observed in the experimental DRIFTS spectra, bridging the gap between experimental data and reaction mechanisms. These findings suggest that both ALs and levulinate-like species can account for the DRIFTS spectrum of ML at the reaction temperature. By combining experimental and computational approaches, this study enriched our understanding of the reaction mechanism, offering insights for future optimization of the catalytic system.

Acronyms

HMF: hydroxy methylfurfural

LA: levulinc acid

LEs: levulinic esters

EtOH: ethanol

ML: methyl levulinate

4-HVA: 4-hydroxyvaleric acid

MV: methyl valerate

2-P: 2-pentanone

EL: ethyl levulinate

AL: angelica lactone

αAL: α-angelica lactone

βAL: β-angelica lactone

GVL: γ-valerolactone

EHP: ethyl 4-hydroxypentanoate

EP: ethyl pentenoates

CTH: catalytic transfer hydrogenation

MPV: Meerwein-Ponndorf-Verley

DRIFTS: Diffuse Reflectance Infrared Fourier Transform Spectroscopy

DFT: Density Functional Theory

PBE: Perdew Burke Ernzerhof

FDM: Finite Difference Method

PAW: Projector Augmented Wave

Index

1. Chapter 1 – Introduction

1.1 Biomass derived compounds

Over the last century, there has been a general improvement in living standards accompanied by a growing demand for energy worldwide. The extensive exploitation of fossil fuels as the main energy resources has caused serious problems such as environmental pollution and global warming. These phenomena have necessarily led to the search for renewable and sustainable energy sources[1]. When it comes to the chemical sector and materials manufacturing, a 2017 BASF survey reveals that only 13% of the 20.8 million metric tons of carbon-based feedstock used to produce organic chemicals came from renewable sources, with the remainder generated from oil (76%), natural gas (10%), or coal (1%)[2]. These numbers show unequivocally that industrial chemistry relies mainly on fossil-based feedstocks.

Nowadays, the depletion of fossil fuels and the rising demand for second-generation renewable fuels have driven research towards alternative energy sources and biomass-based chemical processes. However, significant challenges remain in developing a biorefinery that can economically compete with a petrochemical one, due in part to a lack of fundamental understanding of catalytic conversion processes.

1.1.1 The Principles of Green Chemistry

Until the 1990s, the primary focus in developing new chemical processes was solely on profitability, often disregarding environmental and social considerations. In 1998, Paul Anastas and John Warner established guidelines for sustainable production processes in the chemical industry, focusing on preventing damage rather than mitigating its consequences. This effort gave rise to Green Chemistry and its Twelve Principles[3], listed below:

1) **Prevention** - It is better to prevent waste than to treat or clean up waste after it has been created.

2) **Atom Economy** - Synthetic methods should be designed to maximize the incorporation of all materials used in the process into the final product.

3) **Less Hazardous Chemical Syntheses** - Wherever practicable, synthetic methods should be designed to use and generate substances that possess little or no toxicity to human health and the environment.

4) **Designing Safer Chemicals** - Chemical products should be designed to perform their desired function while minimizing their toxicity.

5) **Safer Solvents and Auxiliaries** - The use of auxiliary substances (e.g., solvents, separation agents, etc.) should be made unnecessary wherever possible and innocuous when used.

6) **Design for Energy Efficiency** - Energy requirements of chemical processes should be recognized for their environmental and economic impacts and should be minimized. If possible, synthetic methods should be conducted at ambient temperature and pressure.

7) **Use of Renewable Feedstocks** - A raw material or feedstock should be renewable rather than depleting whenever technically and economically practicable.

8) **Reduce Derivatives** - Unnecessary derivatization (use of blocking groups, protection/ deprotection, temporary modification of physical/chemical processes) should be minimized or avoided, if possible, because such steps require additional reagents and can generate waste.

9) **Catalysis** - Catalytic reagents (as selective as possible) are superior to stoichiometric reagents.

10) **Design for Degradation** - Chemical products should be designed so that at the end of their function they break down into innocuous degradation products and do not persist in the environment.

11) **Real-time analysis for Pollution Prevention** - Analytical methodologies need to be further developed to allow for real-time, in-process monitoring and control prior to the formation of hazardous substances.

12) **Inherently Safer Chemistry for Accident Prevention** - Substances and the form of a substance used in a chemical process should be chosen to minimize the potential for chemical accidents, including releases, explosions, and fires.

The two chemists' pioneering work has established the foundational principles for building a more sustainable chemical industry. Among these key pillars is the use of renewable raw materials, when technically and economically feasible, as emphasized by principle 7. As a result, much of today's research is focused on advancing the understanding of biomass treatment and conversion processes, and the design of better catalysts.

1.1.2 Biomass and biorefineries

Biomass and biorefineries represent a crucial shift towards sustainable and renewable resource utilization. The essence of biomass lies in its ability to continuously regenerate through natural

processes, making it a crucial component of a circular economy. Biorefineries uses this renewable potential by converting biomass into a range of valuable products, including biofuels, chemicals, and materials, similarly to traditional petrochemical refineries

As a general definition "biomass" denotes organic materials derived from plant or animal sources. In particular, it is categorized into three classes:

First-generation biomass involves agricultural raw materials like sugarcane, potatoes, cassava, corn and others. Using these resources however has led to significant debate and concerns about rising food prices, driven by the large land area required for these crops and their diversion from food production.

Second-generation biomass, such as lignocellulosic materials, appears to be a strong alternative to the first class as it avoids direct and indirect competition with food for human consumption and animal feed and reduce environmental risks, such as soil degradation, while simultaneously valorising waste from other industries, such as agriculture or forestry[4];

Third-generation biomass refers to algae and other microorganisms; it offers high yield potential and can be cultivated in various environments, including those unsuitable for traditional agriculture.

Currently, research has moved beyond first-generation biomass and is making initial strides into third-generation technologies. However, it remains focused primarily on second-generation biomass due to the reasons previously discussed,[4] despite currently only 3-4% of the 150 billion tonnes of biomass produced by nature is utilized by humans for food and non-food purposes[5].

Focusing on second-generation biomass means to deal with lignocellulosic compounds that are the key structural elements of plants and are found in roots, stalks, and leaves. This type of biomass is composed of three main components: cellulose, hemicellulose and lignin (**Figure 1**). The first one is a high molecular weight linear polysaccharide made up of β(1→4)-linked D-glucose units, organized into fibrils and embedded within a matrix of lignin and hemicelluloses[6]. The fundamental units of lignin are held together by a network of inter- and intramolecular hydrogen bonds and van der Waals forces, resulting in a relatively ordered (crystalline) structure[7].

In contrast to the ordered structure of cellulose, the composition and structure of the other two components (hemicellulose and lignin) vary depending on the type of biomass. Hemicellulose has a branched structure that forms an interpenetrating matrix with cellulose through hydrogen bonds and van der Waals forces, with a core structure typically consisting of diverse sugars, including five-carbon sugars (e.g. xylose, arabinose) and six-carbon sugars (e.g. mannose and

galactose). The β(1→4)-linked D-xylopyranosyl residues are often the most abundant motifs. Lignin, on the other hand, is an amorphous, complex aromatic polymer, cross-linked to both cellulose and hemicellulose through a combination of hydrogen bonds, ionic interactions, ester and ether linkages, and van der Waals forces. The presence of lignin in lignocellulosic biomass creates a protective barrier that prevents the destruction of plant cells.[7]

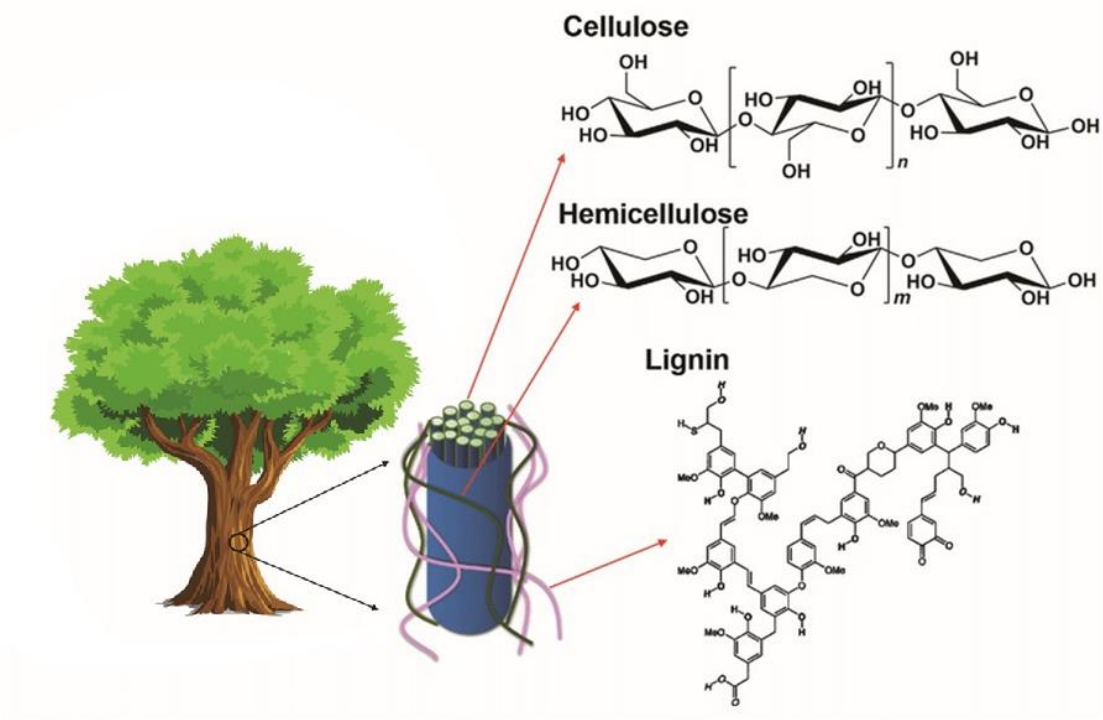

Figure 1 Structure of cellulose, hemicellulose, and lignin in plant cell walls. "Adapted from Lignocellulosic Biomass-Derived Carbon Electrodes for Flexible Supercapacitors: An Overview. Materials. 14. 4571. 10.3390/ma14164571." [8]

The sustainable processing of biomass into a diverse array of marketable products, including food, feed, materials, chemicals, and energy in the form of fuels, power, and heat, is defined as biorefinery. The concept of "biorefinery" encompasses not only the idea itself but also the facilities, processes, plants, or even clusters of facilities involved in the chemical transformations.

Biorefineries can be categorized into several types based on their feedstocks and product outputs. *Phase I biorefineries* primarily focused on utilizing a single feedstock to produce a single main product, such as ethanol derived from corn. In contrast, *phase II biorefineries*, have

evolved to produce multiple products from a single feedstock, exemplifying a more integrated approach to biomass utilization.

The most advanced biorefineries, *phase III biorefineries*, are capable of generating a wide variety of energy products and chemicals from different types of biomass. This diversity enhances the flexibility and adaptability of the refinery within the market.[9]

The IEA (International Energy Agency) classified the processes used in a biorefinery into four groups: (1) mechanical/physical, such as pretreatment, which perform size reduction or a separation of feedstock components without affecting the nature of chemical components of the biomass; (2) biochemical, those processes carried out by enzymes or microorganisms, such as fermentation, anaerobic digestion; (3) chemical, such as hydrolysis, synthesis, hydrogenation and oxidation; (4) thermochemical, where feedstocks are subjected to very high temperature and/or pressure, such as gasification, hydrothermal upgrading, and pyrolysis.

Despite the high production volume, biofuels alone are low-value products, posing significant challenges to achieve the economic objectives of biorefineries when focusing exclusively on biofuel production.[10] Integrating biofuel production with the production of chemicals within a biorefinery framework offers a much higher return on investment, thus meeting both energy production and economic sustainability goals.

1.1.3 Biomass treatment

Significant research efforts are currently devoted to the exploration and the identification of promising chemical processes for converting biomass into organic chemicals.[11] One of the main problem with biomass feedstock is related to its heterogeneity and complexity which imply a difficult conversion. In the valorization of a lignocellulosic biomass, the first step is pretreatment, which aids in the isolation of the cellulose, hemicellulose, and lignin components[12] by opening its structure; lignin is usually removed in a reusable form, the cellulose fibres are decrystallized and the mass transport limitations for a biological or chemical catalyst to be used in successive steps is reduced.

Pre-treatments can be chemical (e.g. acid, alkaline, organic solvents, ionic liquids), physical and/or physicochemical (e.g. steam explosion, wet air, oxidation, ammonia fibres explosion), mechanical (e.g., grinding, chipping, milling), or biological (e.g. microbial, enzymatic). Selecting the optimal pre-treatment method is essential for maximizing product yield and minimizing costs, as pre-treatment can account for over 40% of the total process expenses.[13]

After pretreatment, biomass can be depolymerized using two primary approaches: hydrolysis and thermochemical processing. Hydrolysis breaks down complex polymers into simpler sugars by enzymes or acids, which is essential for further processes like fermentation or chemical conversion into biofuels and biochemicals. Thermochemical processing, by contrast, relies on heat to decompose biomass. Two key techniques in this category are (i) pyrolysis, which heats the biomass in the absence of oxygen to produce bio-oil, syngas, and char, and (ii) gasification, which partially oxidizes the biomass to generate syngas. These intermediate products, whether from pyrolysis or gasification, can then be refined into fuels or chemicals. Both methods are crucial for the valorization of biomass, with the choice depending on factors like feedstock type, desired end products, and process economics. The efficiency and yield of these processes are heavily influenced by the effectiveness of the initial pre-treatment.

Biomass can be converted into a wide array of valuable products, ranging from biofuels like biodiesel to platform chemicals such as lactic acid, furfural, and phenols. Additionally, it can yield bioplastics, solvents, biochar, organic acids, and even specialty chemicals like vanillin and xylitol and natural flavour compounds. Among the most versatile products are bioethanol and levulinic acid. The former, produced through the fermentation of sugars and starches, is used as a biofuel or as a building block for the chemical industry. The latter can undergo various chemical upgrading processes and be used in solvents, plasticizers, and additives.

1.1.4 Bio-ethanol

Ethanol is a two-carbon alcohol with the molecular formula C_2H_6O. At room temperature and pressure, it is a volatile, colourless, and highly flammable liquid. Ethanol is a very versatile solvent, miscible with water and many polar organic solvents, as well as with light aliphatic hydrocarbons.[14] The physical properties of ethanol are primarily due to the presence of the hydroxyl group, which can participate in hydrogen bonding, and the short length of the carbon atom chain. The chemical properties of ethanol are linked to the presence of the hydroxyl group, as many of the reactions in which it participates involve the -OH group.[15]

Currently, ethanol is primarily produced through petrochemical processes, particularly via acid-catalyzed hydration of ethylene. However, due to the economic and environmental issues related to the sustainability of these processes, there is a shift towards greener alternatives, especially those that utilize renewable raw materials.

The bio-ethanol production process depends on the starting raw material, but it generally involves three main steps: (1) obtaining a solution containing fermentable sugars, (2) converting

the sugars into ethanol through anaerobic fermentation (alcoholic fermentation), at the end of which glucose is broken down by certain microorganisms into ethanol and carbon dioxide, and (3) separating and purifying the ethanol, usually by fractional distillation followed by dehydration.[16] For more efficient processes, yeasts are immobilized to enhance their activity and increase the productivity of fermentation.[17] After fractional distillation, an azeotropic mixture consisting of 95.5% alcohol and 4.5% water is produced, which is then dehydrated to obtain "anhydrous" ethanol containing up to 99.6% alcohol and 0.4% water.

Today, large quantities of sustainably produced bioethanol are available at a competitive price, which can be converted into a range of products that complement the basic petrochemical market as well as some specialty products. Globally, approximately 85 million tons of bioethanol are produced annually, with 55% in the U.S., where there is a push for greater fuel independence, and 27% in Brazil, a growing country that has focused on bioethanol as a fuel source.[18]

1.1.5 Levulinic acid

Levulinic acid (LA), molecular formula, $C_5H_8O_3$, is a water soluble, organic compound that features a ketone and carboxylic group giving it a wide range of functionality and reactivity (**Figure 2**).[19] Over the last twenty years, intensive research in the field of biomass valorisation has resulted in the selection of several products called platform chemicals, which can play a crucial role in biorefinery schemes. Among them, LA obtained from the lignocellulosic biomass transformation, and its hydrogenation product, γ-valerolactone (GVL), attracted significant attention.[20] Despite LA can be produced easily and with relatively high yield from acid treatment, its isolation and purification is complex due to LA's high miscibility with liquid. To facilitate the separation process, it has been proposed that unrefined LA is catalytically converted to GVL,[21] which has flexibility as a platform chemical comparable to that of LA and it is sufficiently hydrophobic to allow an energy-efficient separation from its aqueous reaction environment by extraction with a low-boiling acetate followed by facile distillation.

Currently, the production of LA from lignocellulosic biomass involves two main processes, depending on the composition of the raw materials: one process focuses on cellulose and is called direct biomass hydrolysis, while the other, which targets hemicellulose, is known as furfuryl alcohol catalytic hydrolysis.[22] The former is generally preferred due to its greater advantages, like its ability to more efficiently convert cellulose into LA, and it often results in higher yields and fewer by-products. Additionally, direct biomass hydrolysis can be more

straightforward in terms of process optimization and integration into existing bioconversion systems. The proposed mechanisms consist of hexose sugar decomposition to 5-hydroxymethylfurfural (HMF) under acid-catalyzed conditions and include: (1) the hydrolysis of cellulose to glucose, (2) the subsequent isomerisation of glucose to fructose via keto-enol tautomerization, (3) fructose dehydration to hydroxymethylfurfural (HMF) and finally (4) HMF hydration to an equimolar mixture of LA and formic acid. [23]

Once obtained, LA can be utilized to produce a variety of bio-chemicals (**Figure 2**), including succinic acid, resins, polymers, herbicides, pharmaceuticals, flavouring agents, solvents, plasticizers, antifreeze agents, and biofuels or oxygenated fuel additives. Compounds such as γ-valerolactone can be readily blended with petroleum products to create cleaner-burning fuels, offering the advantage of not undergoing phase separation, which prevents contamination with water (as seen with ethanol).

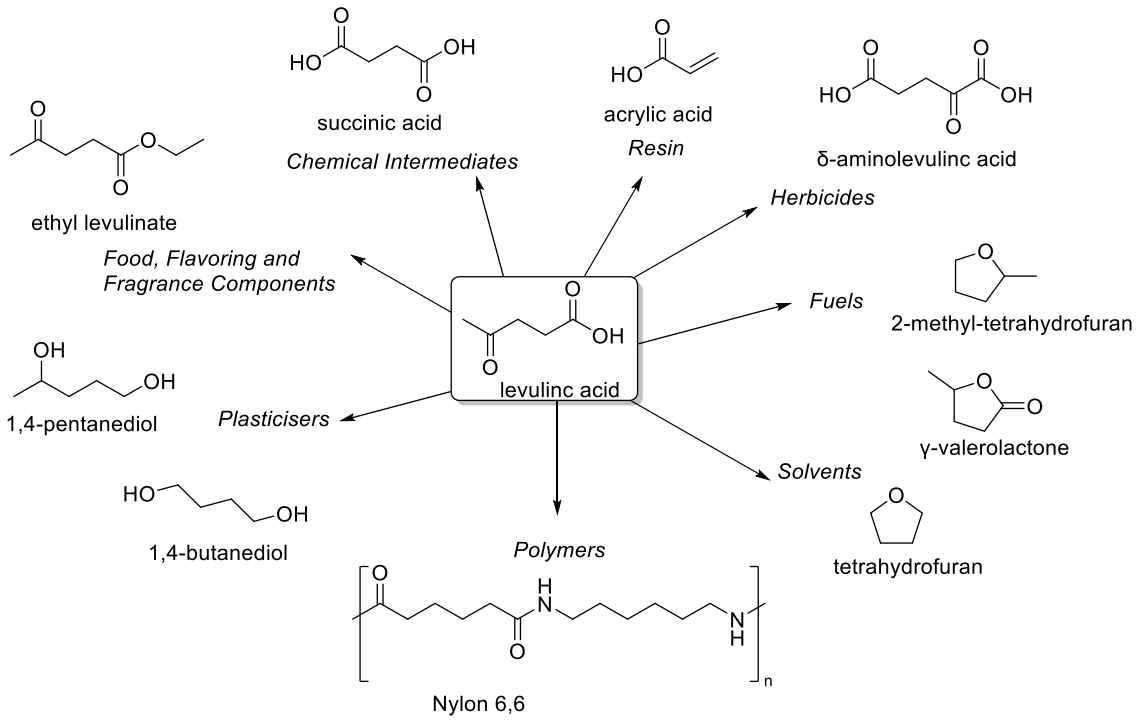

Figure 2 Products and Intermediates Derived from the Conversion of LA.

1.1.6 Esters of levulinc acid

Levulinic esters (LEs) possess distinct physicochemical properties, comparable to those of fatty acid methyl esters[24], which make them versatile for a range of traditional applications in the chemical and process industries, such as solvents, additives for crude oil, flavourings, fragrance

agents, and plasticizers, as well as emerging applications. Additionally, LEs are characterized by low toxicity, high stability, and excellent lubricity, attributes that underscore their potential as fuel additives.[24] Their derivation from renewable feedstocks aligns with sustainability objectives, contributing positively to the green principles of "less hazardous chemical syntheses," "safer solvents and auxiliaries," and "inherently safer chemistry for accident prevention". Esters such as ethyl levulinate (EL) and butyl levulinate (BL) have been successfully tested as oxygenate additives, demonstrating improvements in the lubricity, conductivity, freezing point, and combustion emissions of the fuels into which they are blended.[25] Traditionally synthesized through the esterification of LA with alcohols, these levulinate derivatives can also be directly obtained from cellulose. [26]

1.2 Reduction of LA and LEs to GVL

One of the most versatile product of LA and LEs reduction is GVL. This interesting chemical can be used as a solvent, fuel additive, food additive, perfume making, and adhesives[27]; alternatively it can be converted into valeric biofuels through esterification to pentanoate esters[28] or hydrogenated to pentanoic acid, which can then be catalytically upgraded to 5-nonanone through ketonization and further hydrogenated to produce alkanes or alcohols. These alcohols can be subsequently dehydrated to form alkenes, which can then be oligomerized to enable the production of C_6-C_{27} hydrocarbon fuels[26,28]. GVL formation from LA and LEs has been performed through classical molecular hydrogen reduction, but also the safest CTH has been explored.

1.2.1 Reduction through H_2

GVL can be synthesize through the catalytic hydrogenation of LA to 4-hydroxyvaleric acid (4-HVA) followed by cyclization, or via the acid-catalysed dehydration of LA to α-AL, which is then hydrogenated (**Figure 3**). However, the conventional approach to reducing LA to GVL, typically conducted under liquid-phase and batch conditions, requires the use of molecular hydrogen at high operating pressures (ranging from 5 to 100 bar) and relies on expensive noble-metal catalysts[29]. The hydrogenation process initially forms 4-hydroxyvaleric acid, with subsequent cyclization to GVL driven by elevated temperatures or the presence of an acidic cocatalyst or support. Fine control of the catalyst's acidity and optimization of reaction conditions are crucial to minimize the dehydration of LA to ALs and the subsequent

oligomerization of these unsaturated compounds, which can deactivate the catalyst and reduce process selectivity[30,31].

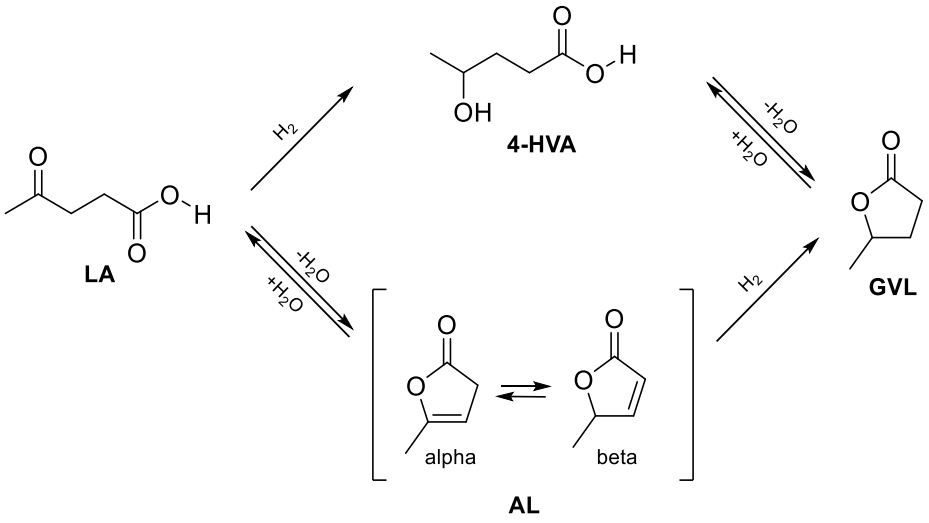

Figure 3 Possible reaction mechanisms for the synthesis of GVL from LA.

The utilization of levulinic esters (LEs) in the synthesis of GVL has attracted significant industrial attention, primarily because of their lower boiling points and the lack of free acid groups compared to LA. Additionally, the alcoholic groups present in alkyl levulinates serve as more effective leaving groups than hydroxyl groups, thereby enhancing the reaction efficiency through a cyclization mechanism.

1.2.2 CTH Reaction: alcohols as hydrogen donor molecules and Gas-Phase reduction

Since the potential of GVL in the bio-based economy, the demand for environmentally friendly and cost-effective production processes is increasingly pressing. Among the most promising methods for performing the reduction is the CTH. This approach uses organic molecules (e.g. alcohols) as reducing agents. The use of an indirect hydrogen source addresses many of the challenges associated with high-pressure molecular hydrogen, such as procurement, transportation, safety risks, and costly infrastructure, thereby enhancing the sustainability of industrial processes. Importantly, a variety of hydrogen donor molecules can now be derived from renewable feedstocks.

Most studies on the CTH of LA and its esters have been conducted in liquid phase using batch reactors, with secondary alcohols (e.g., 2-propanol) as hydrogen donors and zirconia (ZrO_2) as the heterogeneous catalyst.[32] However, these liquid-phase reactions at high temperatures with light alcohols typically require extended reaction times and high autogenic pressures. Our

research group has demonstrated the potential to enhance the CTH of alkyl levulinates using ethanol (and bio-ethanol) in a continuous-flow, fixed-bed, gas-phase reactor, employing high-surface-area ZrO_2. Under these conditions, by operating at 250 °C and atmospheric pressure with a catalyst contact time of just one second, the group has achieved complete conversion of methyl levulinate (ML), resulting in a GVL yield of up to 70%.[33]

Following their investigation of this reaction in the gas phase, our research group hypothesized that the reduction of LA/LE over ZrO_2 leads to a rapid and efficient intramolecular cyclization into the α-AL, which isomerizes into the key intermediate in its β-form (**Figure 4**). This molecule can then undergo consecutive CTH with ethanol, producing GVL. In particular, the proposed reaction mechanism follows an "MPV-like" (Meerwein-Ponndorf-Verley) pathway, where the carbonyl group of the lactone ring interacts with Lewis acid sites on the catalyst surface similarly to the traditional mechanism. However, unlike the conventional concerted mechanism, which involves the direct reduction of the carbonyl group, in this case the reaction exploits the reactivity of α,β-unsaturated carbonyl compounds, in which the double bond is conjugated with the carbonyl moiety. Moreover, the acidic sites on the catalyst can promote the ring-opening of GVL to ethyl 4-hydroxypentanoate (EHP) and subsequent dehydration to form ethyl pentanoates (EP).

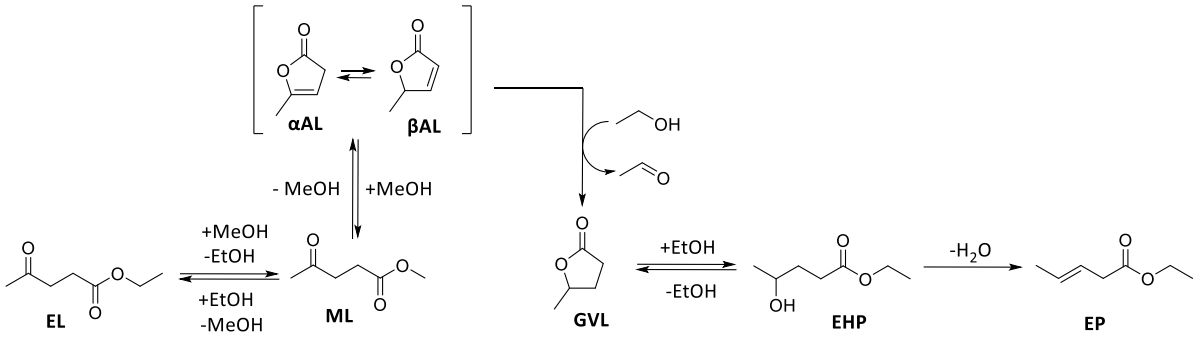

Figure 4 Simplified reaction pathway for the synthesis of GVL from LA by CTH.

Despite the promising results obtained using ethanol as a hydrogen donor for GVL production in gas phase, a gradual deactivation of the ZrO_2 catalyst has been observed. This deactivation is probably due to the build-up of carbonaceous residues on the crucial Lewis acid sites, which

are essential for the CTH process, leading to an increased prevalence of side reactions such as alcoholysis and transesterification (e.g., increased formation of ethyl levulinate (EL) via AL alcoholysis). The carbonaceous residues are hypothesized to be primarily caused by the oligomerization of AL and/or acetaldehyde, but assumption needs to be further investigated.
To gain a more detailed understanding of the proposed mechanism following the experimental findings, computational insights, particularly from DFT calculations, were used to analyse the adsorption properties of the catalyst. These insights suggested that the faster deactivation trends observed in m-ZrO_2 are due to the more rapid accumulation of heavy compounds on the catalytic surface, which results from the higher Lewis acidity and basicity of this crystalline phase. These properties lead also to stronger interactions with the intermediate AL that increases the residence time, thereby making the oligomerization reaction more influential.
Although these computational analyses have enhanced our understanding, the proposed mechanism has not yet been fully validated. Therefore, additional studies utilizing computational methods would be valuable for confirming these hypotheses and providing a more comprehensive understanding of the reaction mechanism.

1.3 Computational insights for biomass catalytic conversion

Mechanistic studies of catalytic reactions can be quite challenging, particularly when dealing with biomass-derived compounds. These molecules often contain multiple reactive groups, leading to numerous potential side reactions, among which oligomerization and polymerization are quite common. Over the past decade, the integration of computational approaches alongside experimental techniques has emerged as a valuable strategy for elucidating catalytic reaction mechanisms. The potential of the *ab initio* modelling for catalysis has been demonstrated in rationalizing experimental trends and in the designing of novel catalysts. By providing mechanistic insights, computational modelling can accelerate the development of heterogeneous catalysts and enable the screening of several potential candidates, through the application of machine learning strategies.[34]

Starting from experimental evidence (e.g., XRD and XAFS), a model of the catalyst surface can be constructed. This can be done using either a slab approach, which assumes an infinitely extended structure, or a cluster model, which represents a structure of finite dimensions. Once the model is established, a quantum mechanics (QM) method is required to compute electronic properties and investigate the reaction pathway. DFT is the most widely used method in computational catalysis, as it offers a good balance between accuracy and computational cost.

The combination of DFT and the periodic slab or cluster models allows for an atomistic "vision" of the reaction on the catalyst, providing the energetics of the reaction pathway, including the transition states, that are almost impossible to be characterized otherwise. *Ab initio* modelling can be then combined with other physical measurements and reactor model to obtain a micro-kinetic model of the reaction.

Overall, these results allow for the rationalization or the prediction of the catalyst's activity and selectivity, which are crucial for selecting the most effective one. With the continuous growth of biomass-based chemicals, research has focused on addressing the intrinsic challenges of modelling for biomass valorization, given the need to create a vast reaction network that could involve thousands of elementary steps.

In literature, various examples can be found where computational methods are employed to explore and validate different concepts in the field of biomass-based chemical valorization. In their 2018 review, Réocreux and Michel focused on several studies about aqueous phase reforming (APR) of biomass, from polyols to CO_2 and H_2O, that has been extensively explored from a computational point of view.[35] Several computational studies have concentrated on Pt(111), showing that C-C splitting in ethylene glycol (EG) and glycerol (GLY) is facilitated when CO is a product of the C-C scission. In other words, a sufficient degree of dehydrogenation must be achieved to allow C-C scission. [35]

With the development of new approaches to better account for van der Waals (VdW) interactions, computational methods have been applied to the valorisation of lignin-based chemicals, such as the deoxygenation of guaiacol on a Pt catalyst. In this case, it was demonstrated that the direct deoxygenation of aromatic oxygenates is impossible, involving barriers of around 250 kJ/mol higher than that of the reactant desorption itself (about 200 kJ/mol). However, deoxygenation of the aromatic ring remains energetically feasible at the ether moiety. [35]

Focusing on the work related to this thesis, literature provides some examples where computational methods offer insights into the conversion of LA to GVL. One such example is the study by Ruppert et al., where the authors investigated the reduction of LA with formic acid using a Ru/C-based catalyst. They observed that the process might be structure-sensitive, and their analysis of the relative adsorption energies of formic acid, levulinic acid, and H_2 suggested that surface poisoning by formate causes delays in LA hydrogenation in the presence of formic acid.[36] Another example is from Siddiqui et al., who focused on a Pt-based catalyst that showed

high conversion and selectivity at low temperatures in a batch reactor with external H_2 in an aqueous medium. DFT calculations allowed to demonstrate the formation of an intermediate that bonds with Pt(111) and undergoes ring formation through C-O coupling.[37]

Thus, computational insights can provide a deeper understanding and further clarification of the reaction mechanism, offering valuable perspectives that complement experimental findings.

1.4 Scope of the thesis

Although previous studies[33,38,39] have provided fundamental insights for the clarification of the reaction pathway of CTH of ML with ethanol on *t*-ZrO_2, the full reaction mechanism has not been clarified yet. In this context the combination of experimental and computational investigations has proven to be a winning approach,[39] as also other examples on biomass conversion reactions have shown.[35]

This thesis involves a combined experimental and computational study of the proposed first step of the CTH conversion: the conversion of ML into ALs. Combining experimental (i.e. catalytic tests, DRIFT spectroscopy) and computational results (i.e. free energy profiles, simulated vibrational spectra), this work aims to: 1) provide insights for the mechanism of ML cyclization to the ALs intermediate; 2) clarify the role of hydroxyl groups on the catalyst surface in the reaction.

The thesis is divided into in the following chapters: **Chapter 2** describes the main computational methodologies used; **Chapter 3** is dedicated to the main experimental methodology adopted, i.e. the DRIFT spectroscopy; **Chapter 4** collects the results and their discussion; finally, **Chapter 5** is dedicated to the conclusions.

2. Chapter 2 – Computational Methods

2.1 Density Functional Theory

DFT is a widely used quantum mechanical method, that provides a way to characterize the electronic structures of many body systems (e.g atoms, molecules and solids). DFT has long been the mainstay of calculations in solid-state physics and chemistry, since the use of approximate functionals was shown to provide a strong balance between accuracy and computational costs. This allowed much larger system to be treated than by traditional *ab initio* methods, while retaining much of the accuracy. DFT is founded on the principle that ground state properties of a many electrons system can be determined by its ground state electron density. Although the Hohenberg-Kohn theorems rigorously establish the validity of the theory, it is only the Kohn-Sham (KS) formalism that makes DFT practically applicable for solving the electronic structures of many-electron systems.[40]

2.1.1 The Hohenberg-Kohn Theorems

The Hohenberg-Kohn theorems represent the foundations of DFT and provide a theoretical framework that underpins the use of electron density as the primary variable in describing the properties of many-electron systems.

First Hohenberg-Kohn Theorem. The first theorem states that the ground-state electron density, $\rho(\mathbf{r})$, uniquely determines the external potential $v(\mathbf{r})$ acting on the electrons. This result implies that all physical observables of the system can be expressed as functionals of the electron density. It is proven by contradiction, showing that no two different external potentials can produce the same ground-state electron density.[41]

Second Hohenberg-Kohn Theorem. The second theorem is an application of the variational principle to the density functional. It states that the functional that delivers the ground state energy of the system, provides the lowest energy (E_0) if and only if the input density ($\tilde{\rho}$) is the true ground state density (ρ_0).[41]

$$E[\rho_0] = E_0 \leq E[\tilde{\rho}] \quad \textbf{(1)}$$

2.1.2 The KS Formalism

The KS formalism is a practical implementation of DFT designed to handle the complexities of many-electron systems efficiently.[42]

KS Equations. The KS approach decomposes the complex many-body problem into a set of non-interacting single-particle equations, by introducing a fictitious non-interacting reference system, that has the same electron density as the real system. In this formalism, the total energy E[ρ] is expressed in terms of the electron density ρ(r) and can be written as:

$$E[\rho] = T[\rho] + \int v_{ext}(\boldsymbol{r})\rho(\boldsymbol{r}) + E_H[\rho] + E_{XC}[\rho]_{\,0} \qquad \textbf{(2)}$$

Here, T[ρ] represents the kinetic energy of the non-interacting system, the second term represents the electron-nuclei interaction (v_{ext}(**r**) is the external potential), E_H[ρ] represents the Hartree energy due to electron-electron repulsion, and E_{XC}[ρ] is the exchange-correlation energy functional, which encapsulates all many-body effects not captured by the other terms. All the terms that appear in **Equation 2** can be explicitly expressed as functional of the electron density, except E_{XC} which exact expression is unknown. The electron density can be defined using the mono-electronic orbitals of the fictitious system (φ_i). The overall expression for the total energy is:

$$E[\rho] = -\frac{1}{2}\sum_{i}^{N}\langle\varphi_i|\nabla^2|\varphi_i\rangle + \frac{1}{2}\sum_{i}^{N}\sum_{j}^{N}\iint |\varphi_i(\vec{r_1})|^2\frac{1}{r_{12}}|\varphi_i(\vec{r_2})|^2\, d\vec{r_1}d\vec{r_2} \qquad \textbf{(3)}$$
$$+\; E_{XC}[\rho(\vec{r})] - \sum_{i}^{N}\int\sum_{A}^{M}\frac{Z_A}{r_{1A}}|\varphi_i(\vec{r_1})|^2 d\vec{r_1}$$

By applying the variational principle to this expression, one can obtain the KS equations:

$$\left[-\frac{1}{2}\nabla^2 + \left(\int\frac{\rho(\vec{r_2})}{r_{12}}d\vec{r_2} + V_{XC}(\vec{r_1}) - \sum_{A}^{M}\frac{Z_A}{r_{1A}}\right)\right]\varphi_i = \left(-\frac{1}{2}\nabla^2 + V_{eff}(\vec{r_1})\right)\varphi_i \qquad \textbf{(4)}$$
$$= \varepsilon_i\varphi_i$$

Self-Consistent Field (SCF) Procedure: The KS equations are a set of single-particle Schrödinger-like equations that can be solved iteratively. The SCF procedure begins with an initial guess for the electron density, which is used to solve the KS equations and obtain a new density. This process is repeated until convergence is achieved, resulting in a self-consistent

solution. It is noteworthy that the expression of E_{XC} is unknown, and this is an important limitation of DFT. Anyway, during the decades more and more sophisticated strategies (i.e. LDA, GGA, mGGA, RPA) have been developed to obtain more accurate E_{XC} that can be applied for reliable calculations.

2.2 Periodic DFT

A solid system could be thought as a "molecule" made up of infinite atoms. In this context, solving the electronic structure of a solid using DFT would entail solving an infinite number of KS equations. Naturally, this approach is impractical. However, for crystalline solids, which exhibit long-range order and translational symmetry, the Bloch Theorem provides feasible solutions. The wavefunctions of electrons in a periodic potential can be expressed as the product of a plane wave and a function that has the same periodicity as the crystal lattice:

$$\varphi_{ik}(r) = e^{ik*r} u_{ik}(r) \quad \textbf{(5)}$$

where u_{ik}(r) has the same periodicity of the lattice, meaning u_{ik}(r+T)= u_{ik}(r), where T is a lattice translation vector. This simplifies the problem of solving the KS equations in periodic systems by reducing the problem to a reduced region (the first Brillouin zone) rather than over the entire space. This implies that in periodic systems the KS equations do not need to be solved everywhere in space but only within the unit cell. This reduction simplifies the computational process significantly. The resulting equation for the periodic part of the wavefunction u_{ik}(r) is:

$$\left[-\frac{1}{2}(\nabla + ik)^2 + V_{tot}(r)\right] u_{ik}(r) = \varepsilon_i u_{ik}(r) \quad \textbf{(6)}$$

This form of the KS equation is essential for calculating electronic band structures in crystalline materials, due to the fact that KS orbitals can be expressed in terms of Bloch functions, which are easier to handle computationally.

2.3 DFT+U

The DFT+U method is an extension of standard DFT that corrects for the self-interaction errors in solid systems with strongly localized electrons, such as d- or f-electron systems. The key idea is to add a Hubbard-like term U to the standard DFT energy functional:

$$E_{DFT+U} = E_{DFT} + \frac{U}{2}\sum_{i,j}(n_i - n_j)^2 \quad \textbf{(7)}$$

This term penalizes deviations from integer occupations of the localized orbitals, thereby correcting the underestimation of the electron-electron repulsion in standard DFT. DFT+U is particularly useful for materials where standard DFT fails to correctly describe electronic correlations, e.g. transition metal-oxides, which are of special interest in the context of heterogeneous catalysis.[43,44]

2.4 VASP

Vienna Ab initio Simulation Package (VASP) is a widely used computational tool for performing quantum mechanical molecular dynamics (MD) simulations and DFT calculations, which are essential for studying the electronic structure of solid state materials and surfaces.[45] VASP employs several tools and smart strategies to achieve accurate and efficient simulations, particularly the plane wave basis sets, the pseudopotentials, and Projector Augmented-Wave (PAW) method.

2.4.1 Plane waves basis set

In VASP all central quantities (e.g. one-electron orbitals, electronic charge density, local potentials) are expanded in plane wave basis set. Plane waves are an ideal choice for periodic systems like crystals because they inherently satisfy the periodic boundary conditions, which simplifies the mathematical formulation of the problem. The use of plane waves also facilitates the calculation of gradients and integrals in reciprocal space (through Fast Fourier Transform), making them well-suited for describing the electronic states in a periodic potential. The accuracy of the calculations can be improved by increasing the plane wave cutoff energy. This parameter determines the size of the basis set, including all plane waves with kinetic energy below the specified cutoff. While raising the cutoff energy generally enhances accuracy, it also increases the computational cost.

Although plane waves provide an effective basis set for expanding the wavefunction in the presence of a periodic potential, they are less suitable for accurately representing the behavior of functions near the nuclei, where the wavefunctions may exhibit multiple nodes. For instance, in **Figure 5** the schematic behavior of a Bloch function of a one dimensional crystal is shown. Accurately capturing this kind of behavior would require an extremely large plane wave basis set. This is where pseudopotentials become essential.

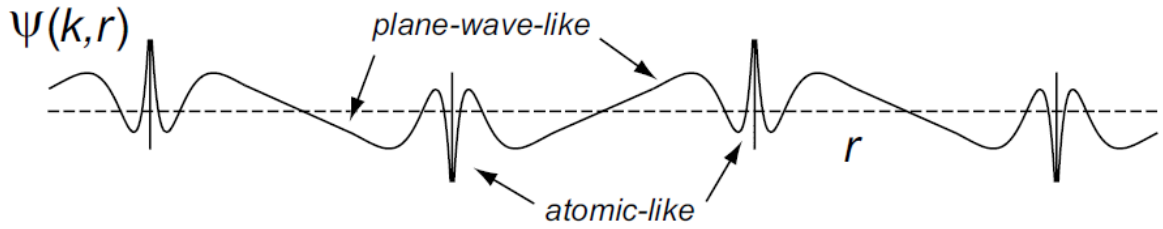

Figure 5 Schematic drawing of a 3s-derived Bloch Function of a one-dimensional crystal of atoms at the X point. Close to the nuclei the function oscillates rapidly, in the bonding region is smooth, and resembles a simple cosine function (plane wave).[46]

2.4.2 Pseudopotentials

Pseudopotentials are used to simplify the computational treatment of electron-ion interactions by replacing the complex interactions between valence electrons and atomic nuclei (along with the core electrons) with an effective potential. This allows for a significant reduction in the computational effort without compromising the accuracy of the calculations for the valence electrons. The pseudopotential can represent the correct behavior in the interstitial region between the atoms, but not near to the nuclei. Using this approach, the valence electrons are described by pseudo-wavefunctions with significantly fewer nodes, making the plane-wave basis set efficient (**Figure 6**). This method assumes that the core electrons are “frozen”, being considered together with the nuclei as rigid non-polarizable ion cores. Therefore, it is assumed that there is no significant overlap between core and valence wave-function

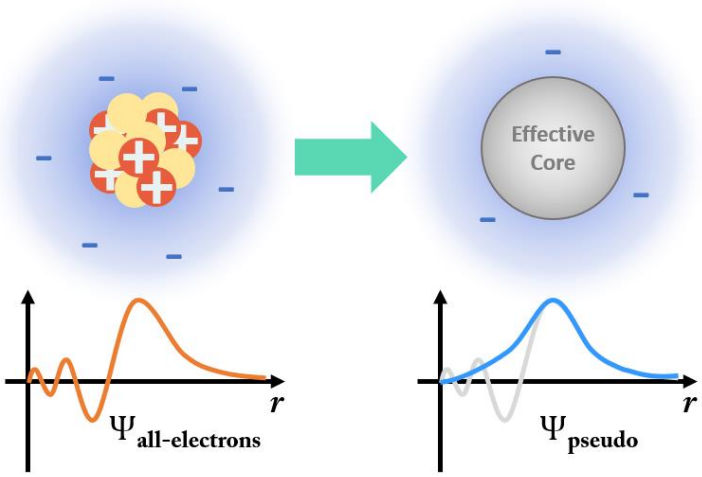

Figure 6 Schematic explanation of pseudopotential method. All-electrons wavefunction is shown (on the left). Through the pseudopotential, a pseudo wavefunction (on the right), that replicates well the behaviour in the interstitial region, but not near to the nucleus, is obtained.[47]

2.4.3 PAW Approach

The Projector Augmented-Wave (PAW) method, introduced by Peter Blöchl in 1994, is a hybrid approach that combines the advantages of the pseudopotential method with the precision of all-electron calculations.[48] In traditional pseudopotential methods, the core electrons are implicitly included in the calculations, and only the valence electrons are treated explicitly. However, this can sometimes lead to inaccuracies, especially in systems where core-valence interactions are significant.[49] The PAW method addresses these limitations by transforming the all-electron wavefunctions into smoother pseudo-wavefunctions that are easier to treat computationally, while still allowing for the reconstruction of the full all-electron wavefunctions as needed. This is achieved by projector functions that map between the pseudo and all-electron spaces. The PAW method is particularly advantageous in calculations involving transition metals, where the core states can play a critical role in the material's properties.

2.5 Computational Modeling of an Heterogeneous Catalyst

In the field of computational heterogeneous catalysis, accurately modelling the interaction between reactants and catalyst surfaces is critical for understanding reaction mechanisms and improving catalyst design. To do so, a proper model of the catalyst and a reliable computational method are needed. As stated in the previous paragraphs of this chapter, DFT is the best

computational method when dealing with many atoms systems. For what concern the modelling of the catalyst, two primary methods are widely used: slab models and cluster models (**Figure 7**). Each of these approaches offers unique advantages and is suited to different types of catalytic systems and research questions.

Slab Models

The slab model is a powerful tool for simulating extended surfaces, which are characteristic of many catalytic materials, particularly in industrial applications. This method involves constructing a periodic model of the catalyst surface, typically representing it as a thin "slab" of the material, which is then repeated infinitely in two dimensions using periodic boundary conditions (PBCs) thanks to solid state software like VASP or Quantum Espresso.

The slab models excel at simulating large, continuous surfaces such as those found in bulk metal catalysts. The periodicity in the slab model ensures that edge effects, which could artificially influence the catalytic properties, are minimized.

This approach allows for the study of various surface-related phenomena, including adsorption of reactants, surface diffusion, and the formation of intermediates. These are critical aspects in heterogeneous catalysis, where the nature of the surface strongly influences catalytic activity and selectivity. This approach enables the study of various surface-related phenomena, including reactant adsorption, surface diffusion, and the formation of intermediates. These factors are crucial in heterogeneous catalysis, where the surface characteristics significantly impact catalytic activity and selectivity. However, this method may not be suitable for catalysts with irregular surfaces or nanoparticulate structures.

Cluster Models

In contrast to slab models, cluster models focus on a finite group of atoms or molecules, representing a localized region of the catalyst. These models do not employ periodic boundary conditions, but use molecular softwares (e.g. Gaussian, Orca), based on localized basis sets.

Cluster models are particularly effective in studying isolated catalytic sites, such as metal atoms supported on oxide materials or small metal clusters. This approach is ideal for investigating reactions that occur at specific sites on a catalyst, such as on the edge of a nanoparticle or at a defect site.

Since cluster models involve a finite number of atoms, they can be less computationally demanding compared to slab models, especially when dealing with small system. In this type

of system cluster models are advantageous, for examples when the catalyst consists of small particles, such as those found in supported catalysts or when studying catalytic processes that are not well-represented by a periodic surface. [50] However, catalytic processes can be significantly influenced by the periodic nature of the catalyst's crystal lattice, which is not accounted for in cluster models. Additionally, when studying interactions involving medium-sized molecules (e.g. transition states for C-C coupling), it is more practical and computationally efficient to use a slab model rather than a cluster.

In conclusion, both models have their respective strengths and limitations. If the goal is to conduct a mechanistic study and to rationalize experimental trends, the kind of model should be selected based on the specific characteristics of the experimental catalyst and the desired simulated properties.

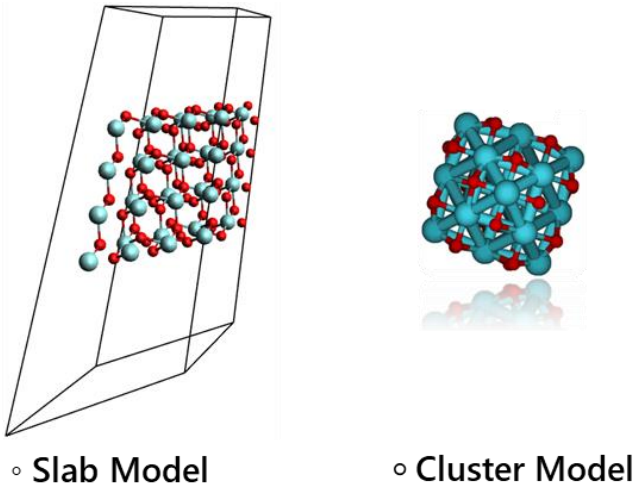

Figure 7 On the left an example of a slab model, on the right an example of a cluster model for a metal oxide catalyst.

2.6 Approaches for simulating vibrations

In mechanistic studies, *in situ* vibrational spectroscopy has proven to be an invaluable tool for investigating molecular structures and reaction dynamics. Computational methods, such as DFT, offer the possibility to simulate molecular vibrations or phonons for extended systems and generate theoretical predictions that can be directly compared to experimental spectra. These computational approaches not only assist in the interpretation of complex spectra but

also enable the prediction of vibrational frequencies and modes for species that are challenging to isolate or detect experimentally. When using a periodic code to simulate adsorbed species, phonon calculations are performed. This calculation relies on the determination of the system's dynamical matrix, which describes how atoms move in response to mutual displacements. The vibrational frequencies, or phonons, are the eigenvalues of this matrix.
If we take a system at the equilibrium, the Hamiltonian of the system can be expressed as:

$$H = \frac{1}{2}\sum_{I\alpha} M_I \dot{u}_{I\alpha}{}^2 + \frac{1}{2}\sum_{I\alpha J\beta} \phi_{I\alpha J\beta} u_{I\alpha} u_{J\beta} \quad \textbf{(8)}$$

where M_I is the mass of the I-th atom, $u_{I\alpha}$ and $u_{J\beta}$ the deviations from the equilibrium positions of the I-th and J-th atoms, and $\phi_{I\alpha J\beta}$ the second order force constant $\left(\frac{\partial E\{R\}}{\partial R_{I\alpha}\partial R_{J\beta}}\Big|_{R=R^0}\right)$
The equation of motion is then given by:

$$M_I \ddot{u}_{I\alpha}{}^2 = -\phi_{I\alpha J\beta} u_{I\alpha} \quad \textbf{(9)}$$

As an ansatz, one can assume that the solution $u_{I\alpha}$ takes the form of a plane wave traveling parallel to the wave vector q. Substituting this ansatz into **Equation 9** leads to an eigenvalue problem:

$$\sum_{J\beta} D_{I\alpha J\beta}(q)\varepsilon_{I\alpha,\nu}(q) = \omega_\nu(q)^2 \varepsilon_{I\alpha,\nu}(q) \quad \textbf{(9)}$$

Where:

$$D_{I\alpha J\beta}(q) = \frac{1}{\sqrt{M_I M_J}} \phi_{I\alpha J\beta} e^{iq(R_J - R_I)} \quad \textbf{(10)}$$

is the dynamical matrix element in the harmonic approximation (i.e. only second order force constant appears). Now, by solving the eigenvalue problem, the phonon modes $\varepsilon_{I\alpha,\nu}(q)$ can be obtained. In principle, an infinite number of equations must be solved, since an infinite number of nuclei compose the crystal. Thanks to the lattice symmetry the infinite system can be reduced to a system of 3p equations (where p is the number of atoms in the basis of the unit cell). The

drawback of this method is that the equations of motion must be solved for each q. This is comparably easy, though, since this scales linearly with the number of $\boldsymbol{q}$ and not cubic like the matrix inversion, and it has to be done only for few $\boldsymbol{q}$ (since the $\boldsymbol{q}$-dependent functions are quite smooth).

The solution of the eigenvalue problem is numerical and implemented within the VASP software. However, before solving the equation to obtain the phonon frequencies and motion vectors, it is necessary to evaluate the force constants. One of the primary methods available in VASP for computing second-order force constants is the finite difference method (FDM).
Let's recall that the total energy of the system (E) can be Taylor expanded around the set of equilibrium positions of the nuclei $\{R^0\}$:

$$E(\{R\}) = E(\{R^0\}) + \sum_{I\alpha} \frac{\partial E(\{R^0\})}{\partial R_{I\alpha}} (R_{I\alpha} - R^0_{I\alpha}) + \sum_{I\alpha J\beta} \frac{\partial E(\{R^0\})}{\partial R_{I\alpha} \partial R_{J\beta}} (R_{I\alpha} - R^0_{I\alpha})(R_{J\beta} - R^0_{J\beta}) + O(R^3) \quad \textbf{(11)}$$

The second derivatives of the total energy with respect to the nuclei positions corresponds to the second-order force constants $\phi_{I\alpha J\beta}$. In FDM, the second-order force constants are computed using finite differences of the forces when each atom is displaced in each independent direction. This simulation requires creation of systems with finite ion displacement of atom α in direction i with magnitude λ , and computations of the orbitals $\psi_\lambda^{uI\alpha}$ and the forces for the systems.

$$\phi_{I\alpha J\beta} = \frac{\partial E}{\partial u_{I\alpha} \partial u_{J\beta}} = -\frac{\partial F_{I\alpha}}{\partial u_{J\beta}} \approx -\frac{\left(F\left[\{\psi_\lambda^{u_{J\beta}}\}\right] - F\left[\{\psi_{-\lambda}^{u_{J\beta}}\}\right]\right)_{I\alpha}}{2\lambda} \quad \textbf{(12)}$$

$$I = 1, \ldots, N_{atoms} \quad J = 1, \ldots, N_{atoms} \quad \alpha = x, y, z \quad \beta = x, y, z$$

Once obtained, these results enable the calculation of vibrational properties, offering crucial insights. Building on this theoretical foundation, we now focus to in situ techniques such as DRIFTS, which facilitate the experimental observation of vibrational modes in real-time under practical conditions.

3. Chapter 3 – Experimental Methods

3.1 DRIFT spectroscopy

The combination of computational simulations with *in situ* vibrational spectroscopy is particularly effective in mechanistic studies. Theoretical predictions open new opportunities to interpretate temperature and time-resolved experimental data.

The DRIFTS is a powerful analytical technique within the vibrational spectroscopy, designed to investigate the surface characteristics of solid materials. The technique operates by directing an infrared beam onto the sample surface, where it undergoes various interactions: part of the radiation is specular reflected, part is absorbed, and part is scattered diffusely through the material. The diffusely scattered light, containing information about the material's absorption properties, is collected and analysed to produce spectra that provide insights into the chemical composition and structural characteristics of the material (**Figure 8**).

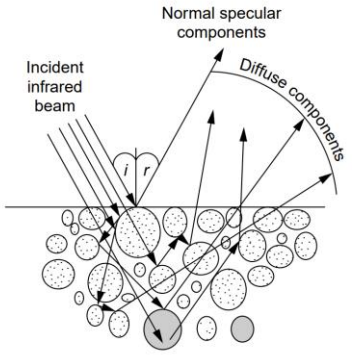

Figure 8 Mechanisms generating the infrared spectrum of a powder.[51]

The fundamental advantage of DRIFTS lies in its ability to probe the surface of catalytic materials under pseudo-operating conditions. This technique is particularly sensitive to surface phenomena, making it ideal for studying catalysts, where reactions occur on the surface. Additionally, it is well-suited for high-temperature or reactive environments, as the DRIFTS setup can include specialized cells that allow for in situ analysis under controlled conditions of temperature and pressure.[51]

Through the observation of molecular adsorbates, reaction intermediates, and surface modifications, DRIFTS allows for a detailed understanding of catalytic mechanisms, which is essential for optimizing catalytic performance and developing more effective materials.[51]

Vibrational spectroscopy enables the direct observation of molecular vibrational transitions, providing valuable insights into the interactions and dynamics occurring within a system.

3.1.1 Instrumental Setup and Configuration of the DRIFTS System

The spectroscopic analyses were performed using a Bruker Vertex 70 spectrometer equipped with a Pike DiffusIR cell attachment. Spectra were acquired with an MCT detector, following 128 scans at a resolution of 4 cm^{-1}. The sample was placed in a crucible, which was subsequently inserted into a heating chamber. Temperature regulation was controlled via a thermocouple coupled with a dedicated control system. A molecular flow was introduced into the apparatus through a pulsed feed system using a syringe. The inlet lines were heated by electrical resistance heaters, maintaining an inlet temperature of 170 °C, and were insulated with glass wool. This setup enabled the vaporization of liquid compounds with suitable boiling points. Helium, serving as the carrier gas, was introduced via a T-valve into the same line, allowing the two gases to flow together into the heating chamber (**Figure 9b**). Inside the chamber, the sample was irradiated by an infrared beam, and the diffusely scattered light was collected and analysed by a detector, as illustrated in the accompanying **Figure 9a**.

Therefore, this particular set-up allows to simulate very well the fix-bed reactor in which this gas-phase reaction normally takes place, and to study how the catalyst behaves *in situ* and in operando conditions.

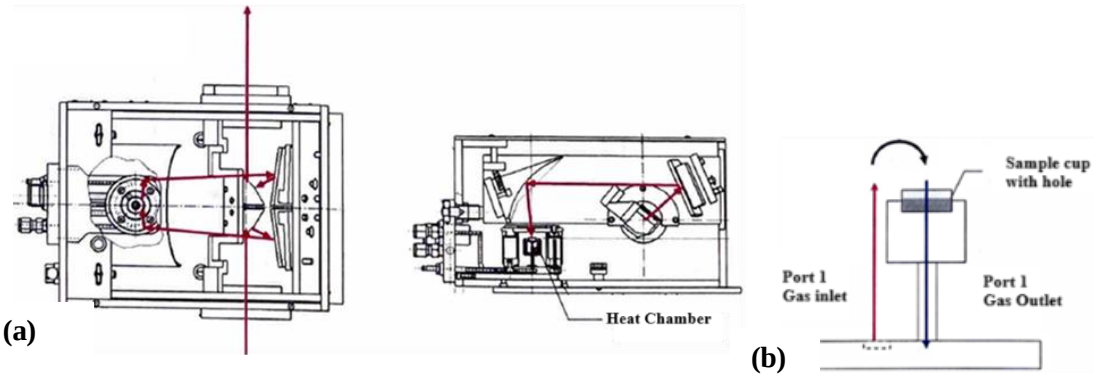

Figure 9 (a) Optical layout and **(b)** gas flow integrated in DRIFT system.

3.1.2 Experimental Procedure for DRIFTS Analysis

The DRIFT instrument enables the execution of experiments in two distinct operational modes: in operando and in situ. In the in operando mode, real-time monitoring of a catalyst or material is conducted under actual working conditions, such as temperature, pressure, and reactant flow, representative of a specific reaction process. Conversely, the *in situ* mode simulates these reaction conditions while introducing a single molecule, offering insights into the behaviour of the catalyst within a controlled environment.

In the initial step for both techniques, potassium bromide (KBr) was placed in the crucible, and a single spectrum was acquired at 250 °C to serve as the background. The system was then cooled to room temperature, and the sample to be analysed was loaded. For all experiments reported in this study, a 50 wt.% mixture of KBr and *t*-ZrO_2 (120 m^2/g) was placed. The sample was pretreated at 500 °C under a flow of air (10 mL/min) for 30 minutes to clean the surface and remove any adsorbed molecules.

In the in operando experiments, the flow was subsequently switched to helium (10 mL/min), and the temperature was lowered to 250 °C, at which point a spectrum of the fresh catalyst was recorded. Following this, a mixture of ethanol and methyl levulinate (molar ratio 10:1) was introduced using a high-precision infusion pump at a flow rate of 1.5 µL/h, in order to obtain a molar composition He : EtOH : ML of 99.9 : 0.09 : 0.01. During the time on steam, a spectra every 5 minutes was recorded to study the interactions between reagents and the surface of the catalyst.

For the *in situ* experiments, after pretreatment, the flow was similarly switched to helium (30 mL/min) while the temperature was lowered to 20 °C. Spectra were recorded during isothermal holds of 10 minutes at the target temperatures. A series of pulses of the molecule of interest (0.5 µL) was then injected over the sample until signal saturation was achieved. Helium was allowed to flow to evacuate weakly adsorbed molecules, while IR spectra were collected at 1-minute intervals to monitor the adsorption process. The system was then reheated to 500 °C, and spectra were recorded at the relevant temperatures, with isothermal holds of 10 minutes.

4. Chapter 4 – Results and discussion

4.1 Previous experimental results: catalytic tests

The fundamental insights crucial to the overall aim of this research have been derived primarily from the catalytic tests previously performed by our groups.[39] In this paragraph the main previous results are summarized.

Tests were carried out by feeding a vaporized ethanol/methyl levulinate mixture (molar ratio 10:1, liquid flow of 0.5 mL/h in a N_2 stream) to a tubular glass reactor containing 1 cm^3 of catalyst with the desired particle size (i.e., 30-60 mesh). Before each CTH test, the catalyst was pre-treated inside the reactor for 2 hours at 400 °C using a 30 mL/min air flow. The output solution collected during the process was sampled and analysed every 50-60 minutes to monitor reactivity during the time-on-stream process. The reaction products were analysed and quantified using a Thermo Focus gas chromatograph equipped with a non-polar capillary column (Agilent HP-5, 5% phenyl-95% methylsiloxane).

The results of the reaction carried out at the optimal temperature of 250°C with a residence time of 1 second on the catalyst composed of tetragonal zirconia (*t*-ZrO_2) are presented below to highlight the observed trends (**Figure 10**). Initially, a good selectivity towards GVL was observed, with a yield reaching 71% after approximately 4 hours of reaction, while the conversion of methyl levulinate remained stable at 100%. During the first 4 hours, GVL was the main product, and its formation was accompanied by the presence of ethyl-GVL, which resulted from a parallel alkylation and CTH reaction. After 4 hours, the conversion began to slightly decline, stabilizing at 94%, with a noticeable shift in the distribution of reaction products: the yield of GVL dropped to just over 20%, while the yield of ethyl levulinate (EL) steadily increased, reaching 55%. This change in chemoselectivity is likely related to an alteration in the nature of the active sites on the catalytic surface, which could become poisoned due to the formation and deposition of heavy organic compounds, thereby promoting the transesterification of ML to EL. Additionally, low yields of ethyl pentenoates (approximately 5%) were observed, suggesting that further CTH reactions on GVL were not favoured under the applied reaction conditions. The production of unidentified compounds, categorized as "Others", remained stable at around 5%.

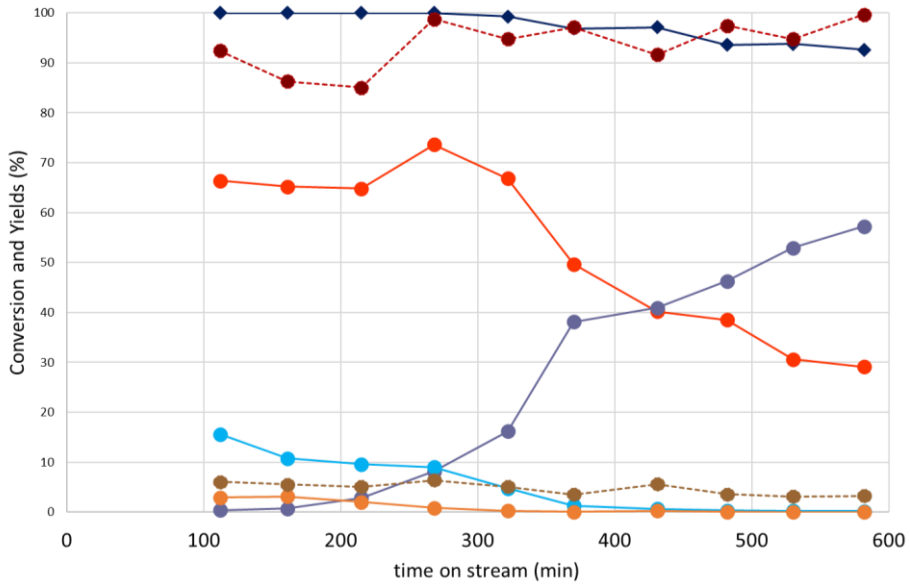

Figure *10* Catalytic results obtained in ML reduction using EtOH as H-donor over *t*-ZrO_2. Reaction conditions: ML:EtOH = 1:10 (molar ratio), T = 250 °C, τ = 1 s, % mol N_2:ML:EtOH = 90.1:0.9:9. Conversion (◆); EL (●); GVL (●); Ethyl GVL (●); αAL (●); βAL (●) EP (●);Others (●);Yields sum/ Conversion (●).[39]

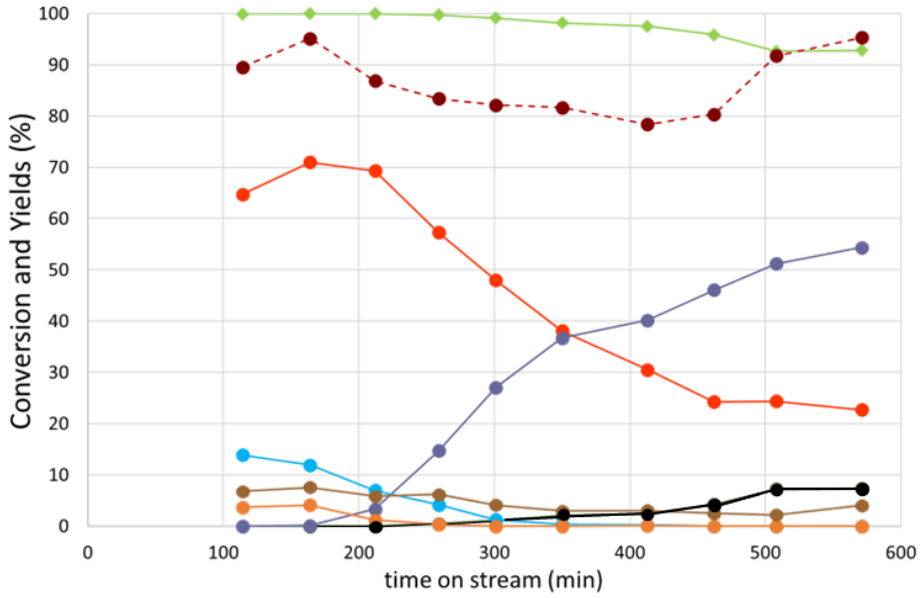

Figure 11 Catalytic results obtained in αAL reduction via CTH using EtOH as H-donor over *t*-ZrO2. Reaction conditions: molar ratio αAL:EtOH = 1:10, T = 250 °C, τ = 1 s, % mol N_2:αAL:EtOH = 90.1:0.9:9. Conversion (◆); EL (●); GVL (●); Ethyl GVL (●); βAL (●); EP (●); Others (●).[39]

From the analysis of additional catalytic tests conducted at various temperatures, the distinct catalytic behaviour of the catalyst became evident, particularly in relation to the accumulation of heavy organic compounds and the yield of GVL. Specifically, *t*-ZrO_2 demonstrated lower efficiency at reduced temperature of 200 °C due to the insufficient activation of CTH reactions. At 300 °C, *t*-ZrO_2 promoted consecutive reactions to ethyl-GVL and other by-products, showing a lower maximum of GVL yield values compared to 250 °C. During the catalytic tests performed with ML, no ALs have been detected (**Figure 10**). To proof if ALs could be a real intermediate of the reaction, readily consumed during CTH step, an additional catalytic test was conducted under standard conditions using αAL instead of methyl levulinate. The results obtained exhibited similar trends to the one of ML, suggesting that αAL might be regarded as a crucial intermediate in ML conversion to GVL (**Figure 11**). It was also revealed the formation of the isomer βAL, that shows the double bond conjugated with the carbonyl function.

The catalyst employed, as previously mentioned, is based on tetragonal zirconia (120 m^2/g), which was prepared using a precipitation method and subsequently calcined in air at 500°C. The catalyst was thoroughly characterized using various techniques.[39] Specifically, the structural phase was confirmed by X-ray powder diffraction (XRD) analysis (**Figure 12**), with patterns collected using Ni-filtered Cu Kα radiation (λ = 1.54178 Å) on a Philips X'Pert vertical diffractometer, equipped with a pulse height analyzer and a secondary curved graphite-crystal monochromator.

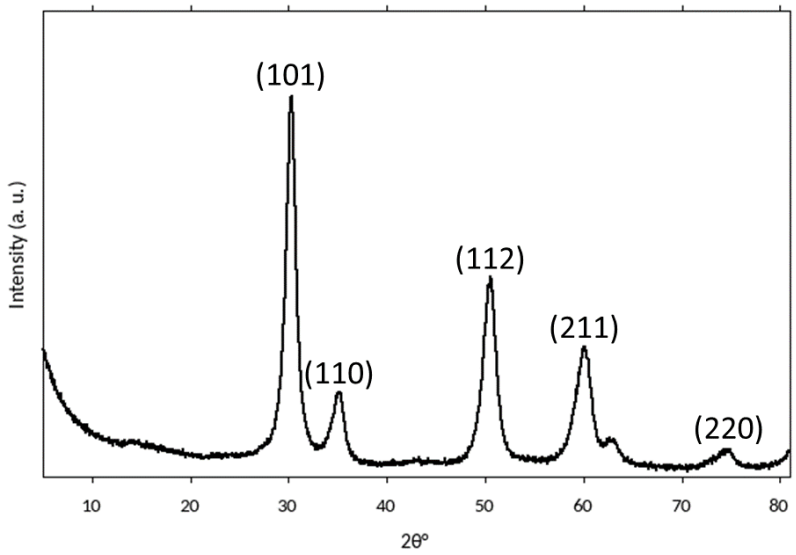

Figure 12 X-ray diffraction patterns for *t*-ZrO_2 catalyst samples.

The surface area of the catalyst was determined through the BET method, measuring the specific surface area via N_2 adsorption-desorption at -196°C using a Sorpty 1750 Fison instrument. For the measurement, 0.1 g of the sample was employed, and it was outgassed at 150°C prior to N_2 adsorption.

Building upon the results from previous studies conducted by the research group, the subsequent investigation aims to examine the behaviour of individual species on the catalyst surface and elucidate the reaction mechanism of ML conversion to αAL in more details. This involves conducting experimental analyses in conjunction with computational studies.

4.2 New experimental results

To elucidate the interactions between the molecules of interest and the surface of the catalyst used, several DRIFT analyses were conducted. A preliminary blank test was performed by loading only KBr into the crucible and following the standard analytical procedures. This test confirmed that KBr does not interfere with the measurements and ensured that no internal or external impurities were present in our experimental set-up that could influence the results.

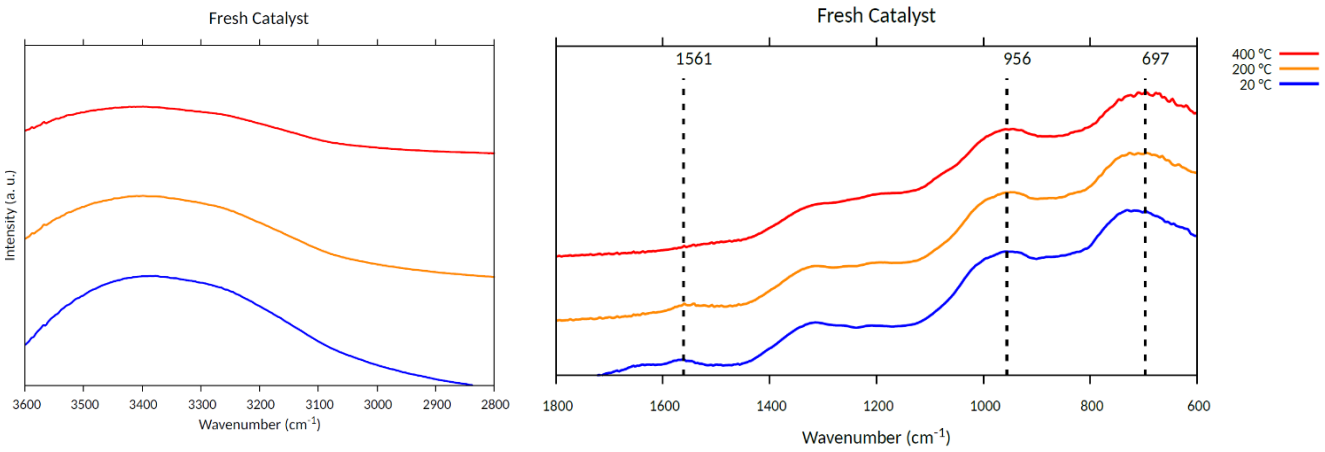

Figure 13 DRIFTS spectra of the catalyst as a function of temperature.

Figure 13 presents the DRIFTS spectra of the bare catalyst obtained during the stepwise temperature-programmed experiment. The spectra are arranged in ascending order of temperature, from the bottom to the top of the graph. A broad band between 3000 and 3500 cm^{-1} is observed, which is attributed to the OH stretching vibrations, likely corresponding to OH groups ("Brønsted acid sites") on the catalyst surface. This assignment is further supported by previous experimental tests involving dimethyl-pyridine adsorption[39]. Additionally, the intensity of this band decreases as the temperature rises.

Given that the sample was pretreated in air at 500 °C, the presence of adsorbed water can be confidently excluded. The signals centred at 697 cm^{-1} are characteristic of the Zr-O bonds in the zirconia catalyst,[52] and are not sensitive to temperature.

An intriguing feature is the appearance of unexpected signals from 1550 cm^{-1}, warranting further investigation. A plausible hypothesis is that these signals are associated with carbonate species due to air exposure, which can be assessed through further DRIFT experiments using CO_2. A notable peak at 950 cm^{-1} could stem from various sources, including impurities, structural defects, or chemical modifications of the material. Previous SEM-EDX (Scanning Electron Microscopy with Energy Dispersive X-ray Analysis) studies conducted on the *t*-ZrO_2 catalyst revealed trace amounts of silicon, approximately 0.5 wt%, likely due to the minor dissolution of SiO_2 from laboratory glassware during the synthesis under basic environment.[39] Therefore, the peak at 950 cm^{-1} can be attributed to the presence of these silicon impurities in the catalyst material.[53] Since DRIFT is highly sensitive to surface phenomena, even such trace impurities can impact the results.

The adsorption of different molecules on *t*-ZrO_2 can result in the formation of various adsorbed species, depending on the surface properties of the material and the temperature. Notably, when working at elevated temperatures, it is important to recognize that (multiple) chemical reactions may be taking place. Our *in situ* experiments were conducted with a single species adsorption on the catalyst, meaning that eventual reactions observed can be due to couplings or decompositions. The use of single species means also that the local concentration of the species in DRIFTS experiments might result higher than the ones using the real reaction conditions tested by our group, however this approach allows to study in a simplified way how the molecules interact with the catalyst. **Table 1** lists some surface species, as simplified models, relevant for our case study, along with their characteristic infrared bands. Obviously some differences in wavenumbers might be observed as compared to the peculiar vibrations, due to a different interaction between the catalyst and the adsorbed molecule[54–58].

Table 11 Characteristics bands of the main surface species that can form after adsorption.

Species		**Characteristic wavenumber (cm^{-1})**	
H-bonded molecular ethanol	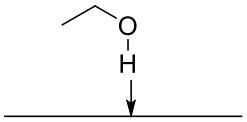	3700-3000 1380 1500-1200	ν(OH) δ(CH_3) δ(CH_3)
O-bonded molecular ethanol	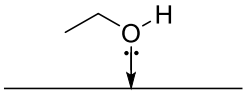	3700-3000 1380 1270	ν(OH) δ(CH_3) δ(CH_3)
Ethoxide	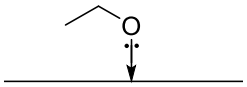	2970 2930 2875 1107 1065 865	ν(CH_3) ν(CH_2) ν(CH_3) $\nu(CO)_{monodentate}$ $\nu(CO)_{bidentate}/\nu(CC)$ ν(CC)
η^1-Acetaldehyde	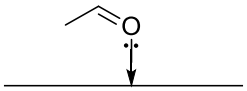	1700-1650 1449-1407 1386-1366 1344	ν(C=O) δ(CH_3) δ(CH) δ(CH_3)
Acyl	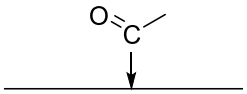	2978 2901 1636	ν(CH_3) ν(CH_2)/ ν(CH_3) ν(C=O)
Acetate	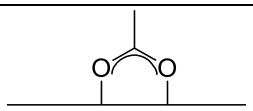	1547 1445 1338	ν_{as}(OCO) ν_s(OCO) δ(CH_3)
Monodentate carbonate	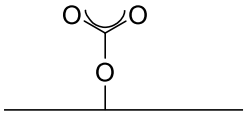	1506 1336	ν_{as}(OCO) ν_s(OCO)
Bidentate carbonate	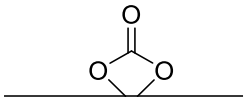	1600-1558 1347-1300	ν_{as}(OCO) ν_s(OCO)

Bridged carbonate	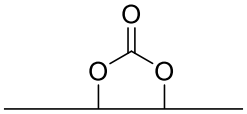	1700 1445 1425 1310	$\nu_{as}(OCO)$ $\nu_{as}(OCO)_{polydentate}$ $\nu_{s}(OCO)_{polydentate}$ $\nu_{as}(OCO)$
Acetone	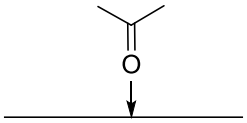	1735-1723 1437-1365 1225-1207	$\nu(C=O)$ $\delta_{as}(CH_3)/ d_{s}(CH_3)$ $\nu(CC)$
Ethyl acetate	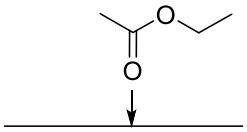	1760-1740 1250-1050	$\nu(C=O)$ $\nu(CO)$
Ethyl but-2-enoate	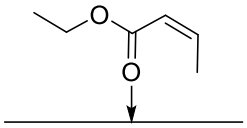	1710-1730 1660-1620 1250-1050	$\nu(C=O)$ $\nu(C=C)$ $\nu(CO)$

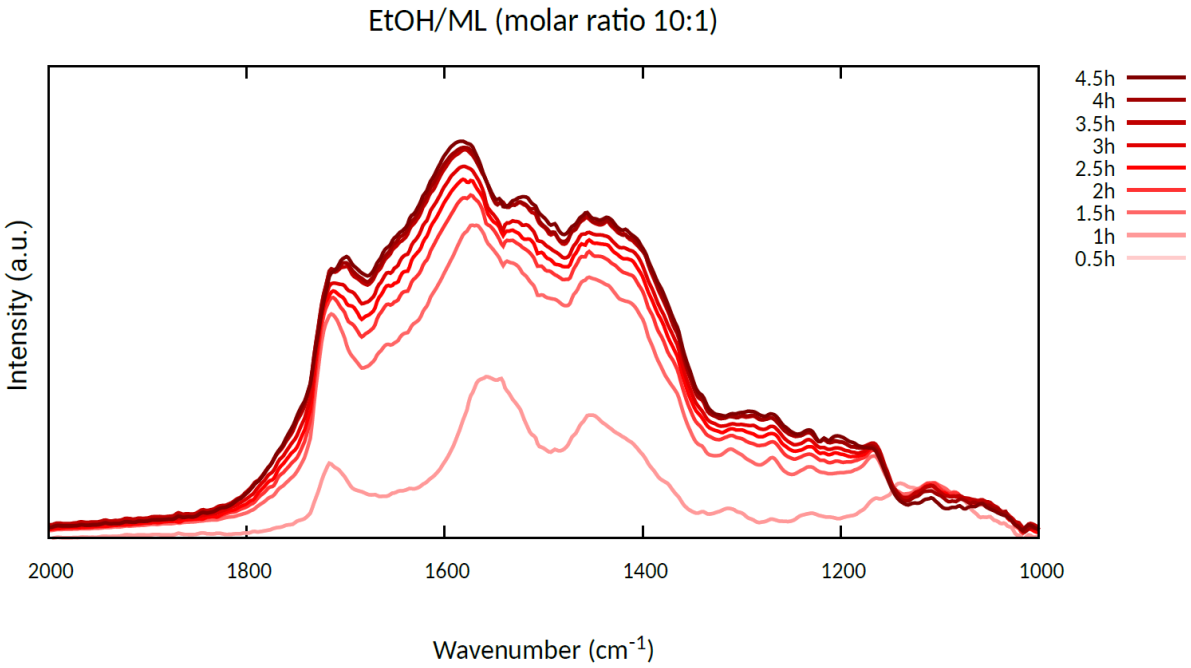

Figure 14 DRIFT spectra of an *in operando* experiment on *t*-ZrO_2, recorded at 250 °C, using an EtOH/ML mixture (molar ratio 10:1).

Figure 14 presents the spectra of the *in operando* experiments recorded at 250 °C every 30 minutes, starting from the initial introduction of the reaction mixture. The mixture consisted of ethanol and methyl levulinate in a molar ratio of 10:1. Analysing the spectra, the first curve recorded after 30 minutes shows a notable peak at 1717 cm^{-1}, which can be attributed to the C=O stretching mode of ML. In the region between 1300 and 1650 cm^{-1}, several unclear signals are observed. These signals increase in intensity throughout the whole time on steam, suggesting that the deactivation of the catalyst might be to an unbalance between the adsorption and the desorption of the molecules at the surface. Due to the complexity and ambiguity of these signals, it was decided to conduct *in situ* analyses on the individual molecules involved to simplify the interpretation of the spectroscopic data. This approach aimed to isolate the vibrational features of each reactant and potential intermediates, providing a clearer understanding of their surface interactions during the reaction.

Attenuated Total Reflectance Fourier Transform Infrared Spectroscopy (ATR-FTIR) was employed to detect the spectrum of the unabsorbed molecule, while DRIFTS was utilized to examine the adsorption mode at room temperature. To gain a clearer interpretation, the spectrum of the bare catalyst was subtracted from that of the adsorbed molecule. This approach was applied to all DRIFTS spectra presented herein. A comparison between the ATR-FTIR and DRIFTS spectra of ML is shown in **Figure 15**.

The bands at 2963 cm^{-1}, 2937 cm^{-1}, and 2879 cm^{-1} in the ATR spectrum were assigned to the $\nu_{as}(CH_3)$, $\nu_{as}(CH_2)$, and $\nu_{s}(CH_3)$ stretching modes of ML, respectively. These signals show minimal changes in the DRIFTS spectrum, as the molecule is not expected to interact with the surface through these groups. In the region below 2000 cm^{-1}, the ATR spectrum clearly displays characteristic peaks for the C=O stretching of the ester (1735 cm^{-1}) and ketone (1714 cm^{-1}) groups. In contrast, the DRIFTS spectrum reveals a single broad peak, which may correspond to either or both functionalities.

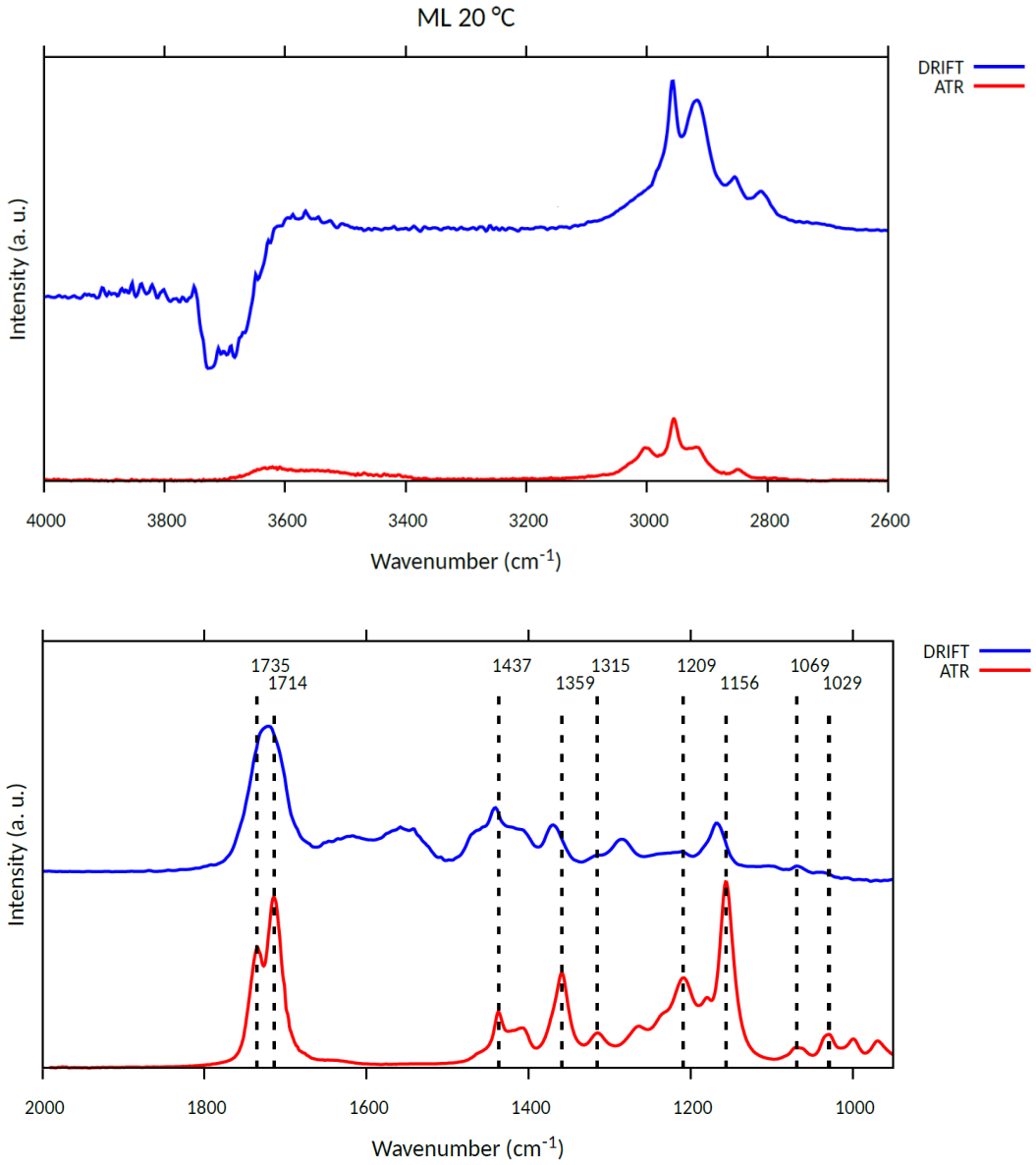

Figure 15 ATR and DRIFTS (on *t*-ZrO_2) spectra of ML recorded at room temperature (r.t.) from 900 to 2000 cm^{-1} (bottom) and from 2600 and 4000 cm^{-1} (top)

Below 1500 cm^{-1}, where C–C stretching and bending modes occur, the spectra remain almost identical to those of the unadsorbed molecule, further indicating minimal interaction with the catalyst surface. However, two low-intensity bands between 1650 and 1500 cm^{-1}, absent in the ATR spectrum, appear in the DRIFTS spectrum. The first band (1650 – 1600 cm^{-1}) is in the typical area of C=C stretching. The second band, centered at around 1558 cm^{-1} exhibit characteristics that in previous studies on valeric acid were attributed to the formation of carbonate-like intermediates[59] (see **Table 1**). Looking at **table 1**, we observe that acetate has really similar frequencies. For this reason, in the next test we define these structures as acetate-

like. Moreover, given that our previous results suggested the conversion of ML into α-angelica lactone (αAL), also this molecule (or its isomer βAL) can be present on the surface, potentially accounting for the band between 1650 cm^{-1} and 1600 cm^{-1}, attributed to its C=C stretching. Additionally, the DRIFTS spectrum shows negative signals in the OH region, suggesting a depletion of surface hydroxyl groups relative to the bare surface. This depletion is likely due to interactions between the molecule and surface hydroxyl groups, a pattern consistently observed with all carbonyl-containing molecules studied in this work. The characteristic C=O peak observed in DRIFTS suggests the physical adsorption of ML on the catalyst during the experiment. However, this observation is not exhaustive, as certain bands appear more perturbed, and new ones emerge. This suggests a preferential chemical interaction between specific functional groups (or chemical bonds) of ML and the active sites of the catalyst. These spectral changes point to a more complex adsorption mechanism involving both physical and chemical interactions, highlighting the catalyst's selective engagement with particular molecular features of the reactant.

These findings suggest that at room temperature ML is predominantly present on the surface as a physically adsorbed molecule, likely interacting through its carbonyl functionalities. However, a small number of acetate-like intermediate (i.e. levulinate), potentially arising from ester decomposition, with two oxygens directly interacting with Lewis acid sites, and interactions with hydroxyl groups, are also present on the *t*-ZrO_2 surface.

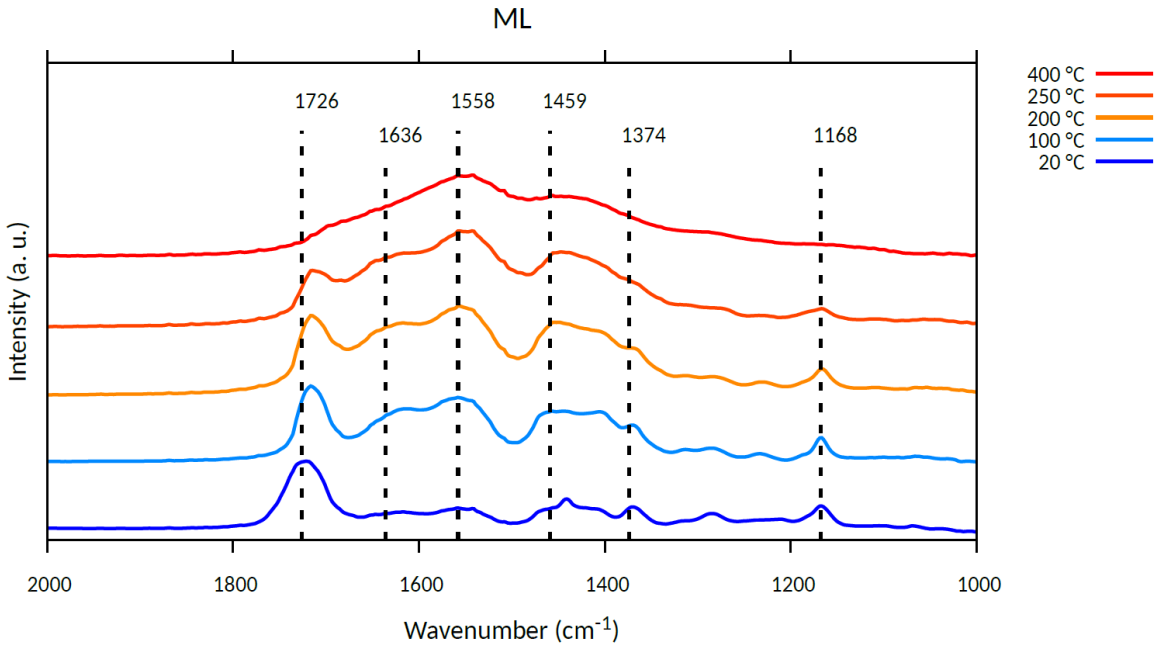

Figure 16 DRIFTS spectra of ML on *t*-ZrO_2 as a function of temperature.

To gain deeper insights into the adsorption process, the evolution of the ML DRIFTS spectrum with increasing temperature was recorded (**Figure 16**). As the temperature rises, the C=O peak shifts from 1721 cm^{-1} to 1716 cm^{-1} and reduces its intensity, while above 300 °C, the C=O stretching band disappears entirely. Simultaneously, the signals between 1650 and 1450 cm^{-1} become more pronounced with increasing temperature, indicating enhanced acetate-like formation at elevated temperatures. Additionally, slight changes are observed in the region below 1400 cm^{-1}, though these are less pronounced compared to other areas.

These observations suggest that at the reaction temperature (i.e. 250 °C), multiple adsorbed species may coexist on the catalyst surface. Alongside physisorbed species which likely decrease in quantity as the temperature increases acetate-like species may also form on the surface. At higher temperatures, the spectrum becomes less defined, likely due to surface reactions such as ketonization or polymerization processes,[52] which may explain the disappearance of the C=O signals and the loss of distinct spectral features. However, the exact nature of all the species formed on the surface requires further clarification. To address this, a deeper understanding of the roles of esters and ketones in this system is necessary. To this end, the spectra of analogous compounds, specifically methyl valerate (MV) and 2-pentanone (2-P), which contain only ester and carbonyl functionalities, respectively were recorded (**Figure 17**). This comparison aimed to shed light on how these functional groups interact with the catalyst surface and contribute to the observed surface interactions and reaction mechanisms. The spectra of all species display a distinct C=O stretching signal at 20 °C. While ML and 2-P exhibit a single band, MV shows a slight shoulder adjacent to the most intense band, though the origin of this feature remains unclear. MV also shows intense signals in the 1650-1500 cm^{-1} region, even at this relatively low temperature, suggesting the presence of both physisorbed ester and acetate-like species, which indicates a complex interaction with the catalyst surface. In contrast, ML, as previously discussed, only displays low-intensity signals in this region compared to its C=O stretching band. Lastly, 2-P shows no signals in this area at room temperature. These observations suggest that the signals in the 1650-1500 cm^{-1} region are likely due to the interaction between the ester functionality, which is absent in 2-P, and the *t*-ZrO_2 surface. This supports the hypothesis that acetate-like formation is linked to the ester functionality, which may be the most interacting group in ML adsorption, while just poor interaction takes place with the carbonyl group at room temperature.

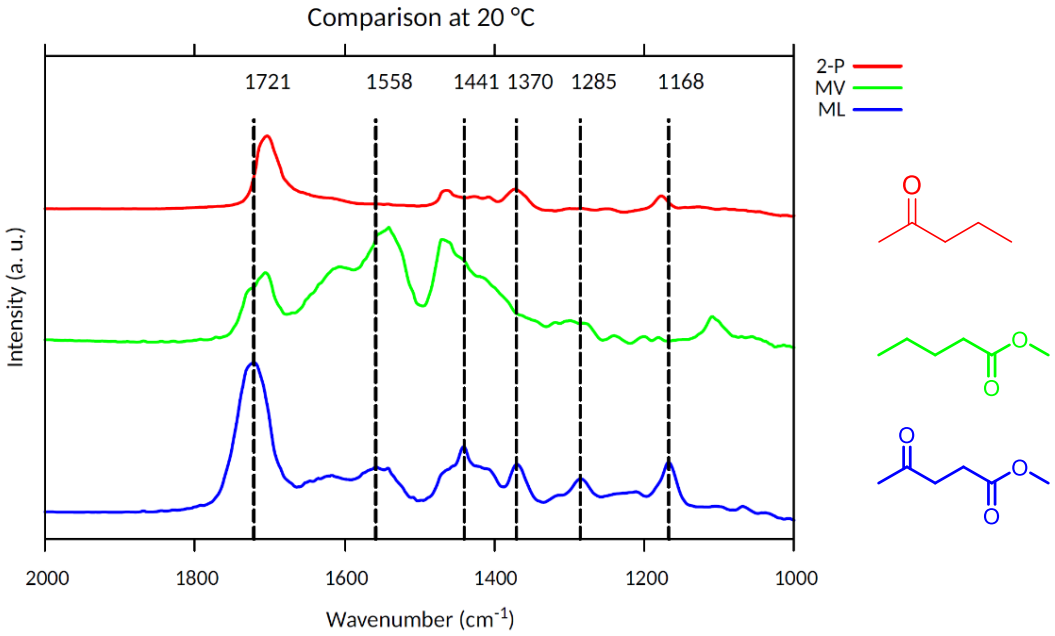

Figure 17 DRIFTS spectra of ML, MV and 2-P recorded at 20 °C.

The evolution of the methyl valerate MV spectrum with increasing temperature further supports our conclusions (**Figure 18**). Notably, at 50 °C, the C=O stretching signal disappears completely, indicating that the ester no longer contributes to the observed spectral features at this temperature. Interestingly, a similar behavior is observed for ML, but only at temperatures above 250 °C. In the case of MV, acetate-like species become the dominant spectral components starting at 50 °C, as evidenced by the increased intensity of signals in the corresponding region. This growing prominence of acetate-like species at elevated temperatures suggests a shift in the ester's interaction with the catalyst surface, with the ester primarily contributing to acetate-like formation, which ultimately becomes the dominant surface species as the temperature rises, potentially accompanied by oligomerization reactions. The comparison of the C=O stretching behavior of MV with that of ML suggests that much of the C=O signal observed for ML at lower temperatures might be not derived from its ester group. This band shifts its maximum from 1726 cm^{-1} to 1716 cm^{-1} as the temperature increases. Two main hypotheses can be proposed for the origin of the C=O stretching signals of ML at relatively high temperature. It could be linked to another product formed, such as αAL, which cannot form from MV. Alternatively, it could be related to ML's ketone group. In fact, we can assume that at low temperatures both physisorbed and acetate-like intermediates are on the surface. While the first one should show both the signal of the ester and the ketone stretching, the second one involves a strong interaction of the ester group with the surface, meaning that only the

ketone stretching should be observed. As soon temperature increases more acetate-like could be formed as the increase of intensity for the 1650-1500 cm^{-1} bands suggest. So, possibly just the ketone will be observed (explaining why the maximum of the band shifts). For this reason, investigations into the behavior of the ketone functionality of 2-P at high temperatures (**Figure 19**) could provide insights into this question. At 20 °C, the spectrum shows a clear CO signal, but no signals in the carbonate/ acetate region. Signals in this area only begin to emerge above 150 °C, when the CO signal disappears. This suggests that reactions involving CO are occurring, but with higher activation energy compared to the degradation of the ester to acetate-like species. Anyway, in this case the band between 1650 – 1600 cm^{-1} is always less pronounced as compared to the esters, indicating that different species are formed in the ketone's case.

The comparison between the pentanone and methyl valerate spectra further supports this interpretation. The CO group from the ester begins forming acetate-like species as early as 20 °C, while the CO group from the ketone does not seem to participate in surface reaction until the temperature exceeds 150 °C.

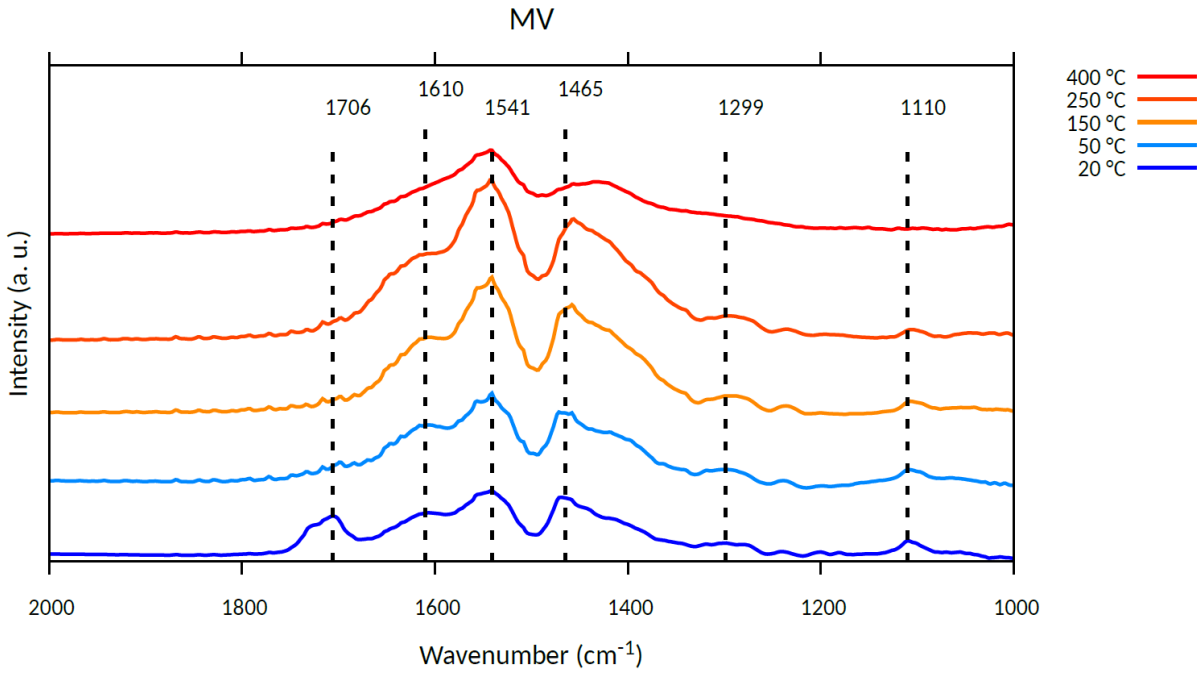

Figure 18 DRIFT spectra of MV as a function of temperature.

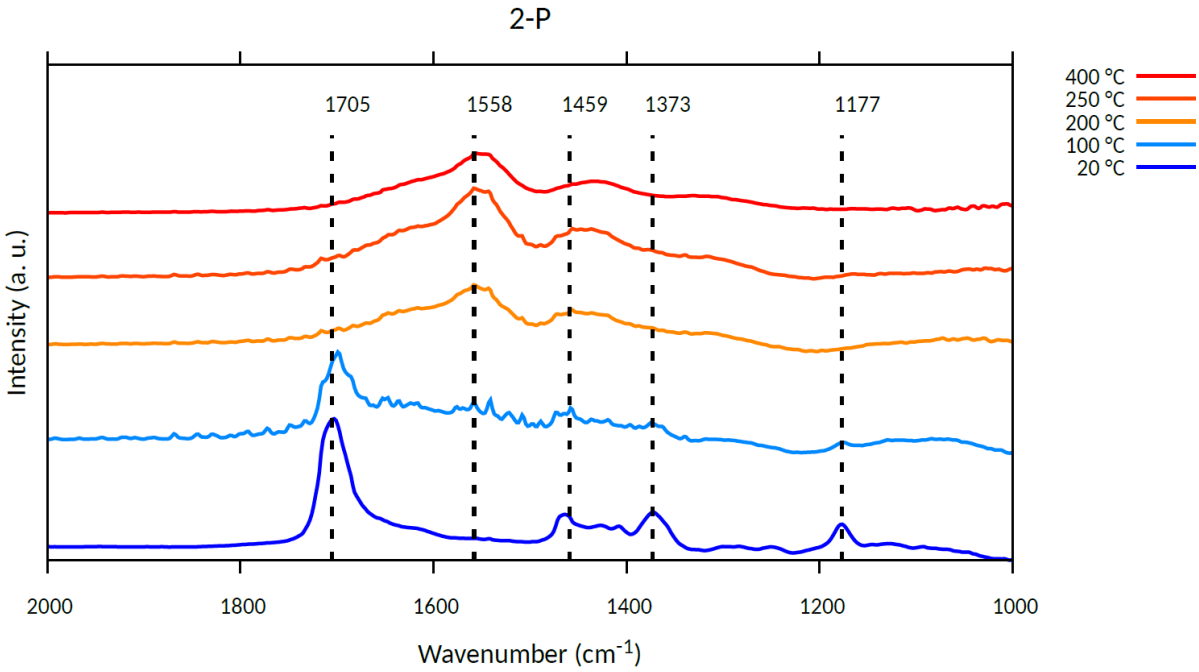

Figure 19 DRIFT spectra of 2-P as a function of temperature.

This behaviour indicates a clear distinction between the adsorption characteristics of the ester and ketone. While the ester decomposes or transforms at relatively low temperatures, leading to the disappearance of its CO signal, the ketone remains adsorbed for a longer period, partly contributing to the CO signal observed in the ML spectrum at higher temperatures. Anyway, ML shows the signal till 250 °C. It could still be regarded as the ketone group. The reason why this signal is observed till higher temperature than 2-P, can be found into the geometry of the acetate-like species; in fact, this would be attached through the ester group to Lewis acid centers over the surface, while the ketone functional group is characterized by a lower interaction with the surface (since it's far from it). On the contrary, in the case of 2-P, the carbonyl group is directly interacting with the Lewis acid sites of the catalyst. Also, some other species might be responsible for it. It might be linked therefore to the ALs, that was proposed as a possible intermediate of the reaction, coming from MeOH elimination and cyclization of ML. For this reason, we decided to study the adsorption of the commercial αAL.

The evolution of the αAL spectrum as a function of temperature reveals behaviour like that of other esters, such as MV (**Figure 20**). At 20 °C, the αAL spectrum displays a characteristic CO stretching signal with a subtle shoulder, such as MV, accompanied by prominent signals in the 1650-1500 cm^{-1} region. Again, these spectral features likely indicate a mixture of physisorbed species and acetate-like species, potentially arising from the partial opening of the αAL

structure at low temperatures. As the temperature increases, the intensity of the bands in the 1650-1500 cm^{-1} range also intensifies, a pattern that is consistently observed across all the esters studied so far. This evidence could suggest that not only closed form of the molecule, but also open forms are present on the surface, and favoured by high temperatures. Interestingly, at 100 °C, a new peak appears at 1719 cm^{-1}. This peak could suggest a temperature-driven isomerization process, where the αAL molecule begins to undergo structural rearrangements, transforming into β-AL. Simultaneously, the other CO stretching signal progressively weakens as the temperature rises, until it nearly vanishes by 250 °C. This disappearance might imply that by 250 °C, only the β-AL isomer remains physically adsorbed on the catalyst surface, together with acetate-likes species, arising from the opening of the ring. Anyway, the CO stretching disappears when further increasing temperature, exactly as the case of ML.

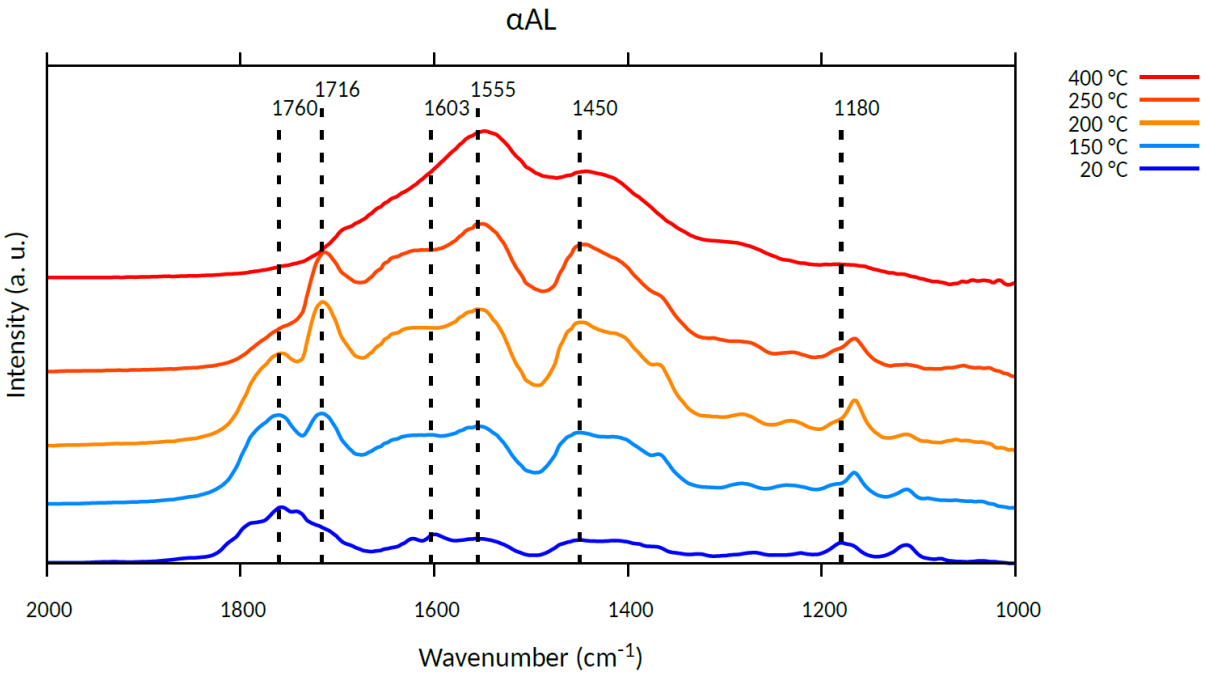

Figure 20 DRIFT spectra of αAL as a function of temperature.

At 250 °C, the CO stretching frequency observed for methyl levulinate (ML) closely matches that of the αAL sample, and the overall spectra of both compounds show striking similarities (**Figure 21**), even appearing superimposable. This raises fundamental questions. One possibility is that ML is fully converted into βAL at 250 °C. Alternatively, it could be hypothesized that, as the temperature increases, αAL begins to revert back to ML, particularly into an acetate-like form (e.g. levulinate).

Although the signals at 1650-1600 cm^{-1}, common to both αAL and ML in their DRIFT spectra, could be attributed to C=C stretching in the ALs, it's worth noting that these signals are identical

to those exhibited by MV (**Figure 17**), a compound that cannot be converted into an AL-like structure. Therefore, the reason for the superimposability of the two DRIFTS spectra at 250°C remains unclear. At room temperature, the DRIFT spectra of ML and αAL also display really different features. For ML, the band in the 1650-1600 cm^{-1} region retains the same characteristics as at 250°C, albeit with lower intensity. In contrast, for the αAL sample, a more structured band with two low-intensity peaks (possibly indicating C=C stretching of the two AL isomers) is observed (**Figure 22**).

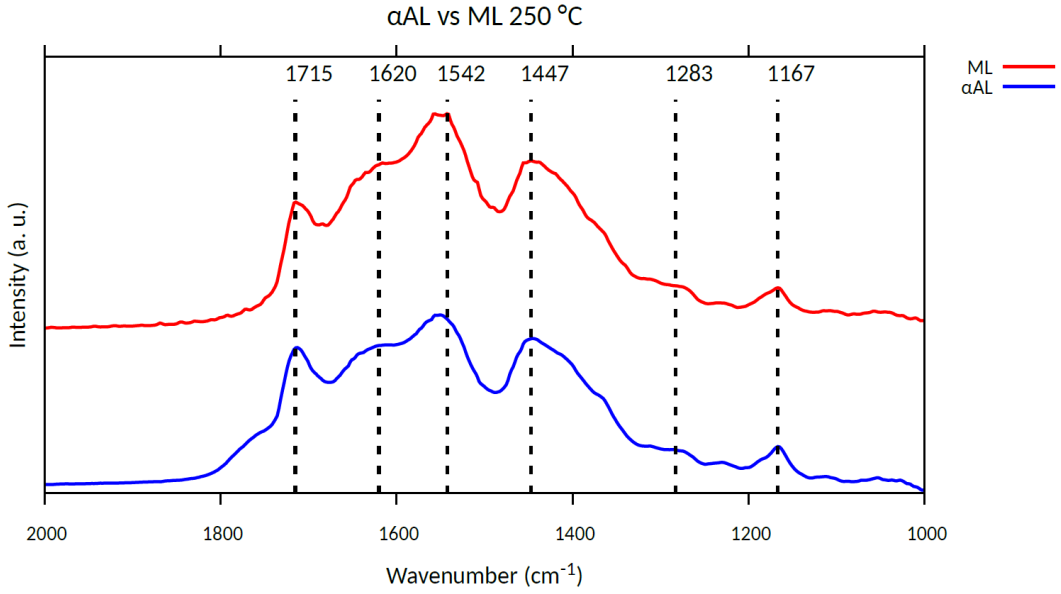

Figure 21 DRIFTS spectra of αAL and ML recorded at the reaction temperature (250 °C)

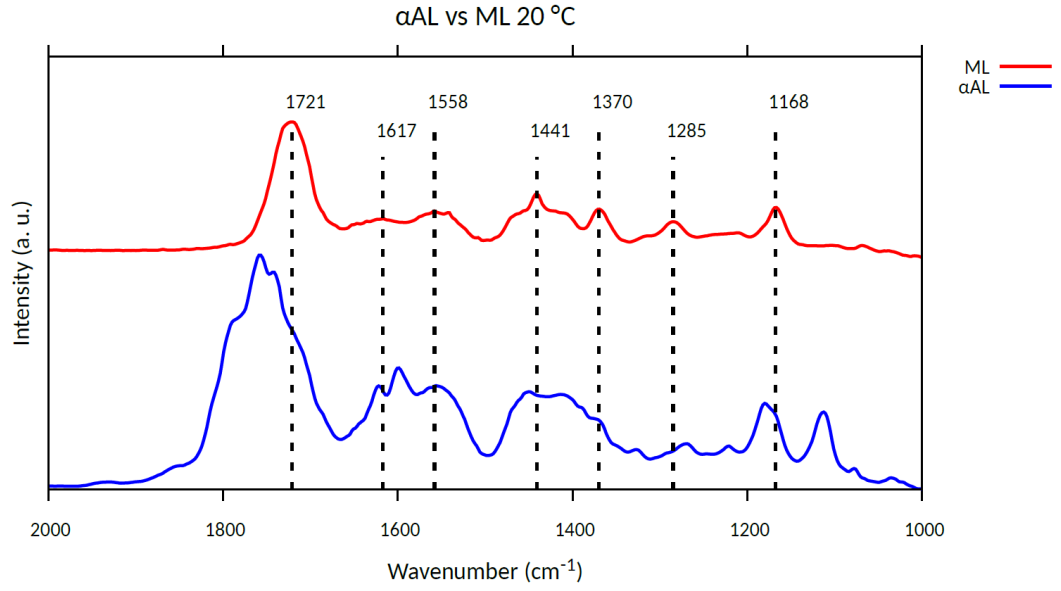

Figure 22 DRIFTS spectra of αAL and ML recorded at 20 °C

In conclusion, the experimental DRIFTS spectra have provided valuable insights into the adsorption of methyl levulinate (ML) on *t*-ZrO_2 and its potential transformation into ALs. The appearance of signals in the 1650-1500 cm^{-1} region for ML at 20 °C, which are absent in the ATR spectrum of the molecule in solution, suggests that in addition to physisorption, a stronger chemical interaction occurs with the surface. This interaction likely involves surface hydroxyl (OH) groups and may lead to the formation of acetate-like intermediates. As the temperature increases, these intermediates become more prominent, while the signals for ML's CO stretching progressively diminish, disappearing entirely by 300°C.

By examining the behavior of MV and 2-P, we inferred that the formation of acetate-like species likely results from interactions involving the ester group, facilitated by the surface hydroxyl groups of the catalyst. These OH groups appear to be depleted compared to the bare catalyst. To explain the persistence of the ML CO stretching signal at higher temperatures, unlike MV and 2-P, we propose that ML's ketone group interacts weakly with the surface, as expected for acetate-like species due to geometric factors, or that ML may be converting into another species, potentially ALs, as the temperature rises.

However, the DRIFTS spectra of α-AL present unclear information. When considering their temperature evolution, this could indicate a temperature-driven transformation involving the isomerization of α-AL to β-AL, or possibly its reversion back to levulinate species.
To better understand the chemical nature of the species formed on the surface and the conversion of ML to α-AL, computational investigations have been conducted.

4.3 Computational results

As an initial step, convergence tests were performed on the unit cell of *t*-ZrO_2 to determine the appropriate energy cutoff (ENCUT) and k-point mesh. The energy cutoff indirectly controls the size of the basis set, while the k-point mesh defines the density of sampling points in the reciprocal space. As commonly done in literature, the energy-per-atom of the unit cell was used as the convergence criterion, with a threshold set to 1 meV/atom. After these tests, an energy cutoff of 600 eV and a Γ-centered k-point mesh of 8x8x7 were selected. The Perdew-Burke-Ernzerhof (PBE) functional was employed to describe the system. To better account for the electronic structure of the solid, the DFT+U method, as implemented by Dudarev et al.[43], was applied. While we did not explicitly calculate the U parameter, we adopted a U value of 4 eV for the Zr d-electrons, based on values reported in literature[60,61]. As expected, the introduction of the Hubbard U parameter resulted in an increase in the band gap from 4.04 eV to 4.39 eV.
With these parameters established, the bulk structure of tetragonal zirconia was optimized, starting from the reference structure available in the Materials Project database[62]. Both atomic positions and lattice vectors were optimized, yielding values consistent with those reported in literature[63]. Once the bulk structure was optimized to its minimum energy configuration, the next step involved constructing a slab model. The slab was generated by cleaving the optimized bulk structure along the (101) crystallographic plane, identified as the most thermodynamically stable through X-ray diffraction (XRD) analysis of our catalyst sample (**Figure 13**). To avoid dipole effects, the slab was set symmetric. A p(3x2) supercell was constructed to ensure that the adsorbed molecules were at least 4 Å away from their periodic images, eliminating spurious interactions. At this point, it was necessary to define the number of layers, the vacuum thickness, and the k-point mesh. To do so, we studied the convergence of NH_3 adsorption energy, a well-documented system in literature[39,64]. Using only the Γ-point, we observed convergence with four fully relaxed layers, obtaining an adsorption energy of 1.15 eV, in agreement with values reported in literature. Increasing the k-point mesh or the vacuum thickness beyond 20 Å did not significantly change the results. We also tested the effect of symmetrizing the adsorbed molecule, but we found no significant differences between the symmetric and non-symmetric configurations, confirming that symmetrizing the adsorbate was unnecessary (**Table 2**). Thus, a p(3x2) supercell with four free layers and a vacuum gap of at least 20 Å was chosen. To further validate the model, adsorption tests with CO were conducted. These tests, under similar conditions, were consistent with the literature values for CO adsorption, fully validating the model (**Table 2**).

Table 2 Energy adsorption of the probe molecules.

NH_3 Adsorption				CO Adsorption	
n° Layer	**Kpoints grid**	**symmetrization**	**ΔE_{ads}/ eV**	**ΔE_{ads}/ eV**	**ν_{CO}/cm^{-1}**
4	1x1x1	no	-1.16	-0.53	2126
5	1x1x1	no	-1.164	**Reference**[65]	
6	1x1x1	no	-1.17	**ΔE_{ads}/ eV**	**ν_{CO}/cm^{-1}**
4	2x2x1	no	-1.10	- 0.50	2127
4	3x3x1	no	-1.10		
4	4x4x1	no	-1.10		
4	1x1x1	true	-1.12		
Reference[66]					
n° Layer	**Kpoints grid**	**symmetrization**	**ΔE_{ads}/ eV**		
4	2x2x1	no	-1.20		

Using the validated model, the adsorption of the molecules of interest onto the bare catalyst surface was investigated. Different adsorption modes for each species were explored, aiming to identify the most stable configurations. The adsorption energies, computed and presented here, are only the electronic energies (that is a good approximation of the enthalpy change), without accounting for entropic contributions.

Beginning with the adsorption behaviour of ML, the molecule preferentially adopts a flat adsorption mode. This geometry corresponds to a physisorbed state (**ML_1**), showed in **Figure 23a**, where the carbonyl oxygen of the ester group coordinates to a Zr^{4+} Lewis acid site. The adsorption energy for this configuration is strongly exothermic, by -1.18 eV, and only minor geometrical distortions are observed. The C=O bond shows no elongation, and a distance CO-Zr of 2.96 Å is observed. When the molecule is brought close to the surface, a second adsorption mode is observed, leading to the formation of a levulinate-like structure **ML_2** showed in **Figure 23b**. This species is thermodynamically more stable, with a more exothermic adsorption energy of -1.89 eV. In this case, a strong distortion of the molecule and of the surface takes place. The ester oxygen atoms coordinate to two adjacent Zr atoms on the catalyst surface, while the carbonyl carbon binds to a bridging oxygen atom of the surface. This interaction

results in the elongation of the OC-OCH_3 bond of the ester group (+15% in bond distance), with the bridging oxygen greatly distorted from the bare catalyst surface.

The adsorption behaviour of αAL follows a similar trend. Like ML, geometrically distorted form of αAL is energetically more favourable. In this case the ring is opened, due to a strong interaction of the bridging oxygen of the surface with the carbonyl carbon leading to a bidentate intermediate. The obtained structure, **αAL_2**, **Figure 24a** has an adsorption energy of -2.65 eV. In contrast, the physiosorbed state of αAL, **αAL_1**, **Figure 24b**, where the carbonyl oxygen coordinates to a Zr^{4+} site, is less exothermic, with an adsorption energy of -0.86 eV. The same behaviour was observed also for βAL (with adsorption energies of -0.80 eV for the closed form and -2.04 eV for the open form, respectively). The opening of **ALs** appears to be highly exothermic. Anyway, although thermodynamics appears favourable, to have a clearer insight into the feasibility of the opening process, the activation barrier must be computed, and the entropic effects included. Finally, we also studied the adsorption modes of the final product, GVL. As the case of ALs, it features two different adsorption modes, a closed (**GVL_1**) and an open form (**GVL_2**), with adsorption energies of -0.84 eV and -2.35 eV (**Figure 25a** and **Figure 25b**), respectively, in lines with the ones of ALs.

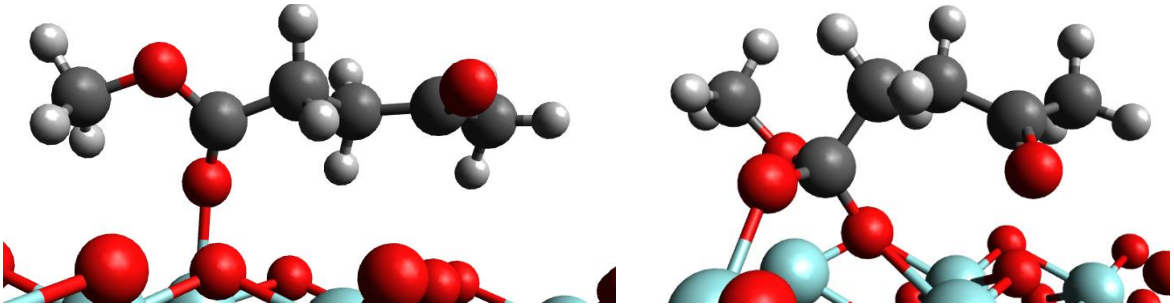

(a) **(b)**

Figure 23 Side view of optimized minimum-energy configurations of ML adsorbed on the catalyst surface. The species **(a) ML_1** represents the physisorbed version, while **(b) ML_2** depicts the carbonated form.

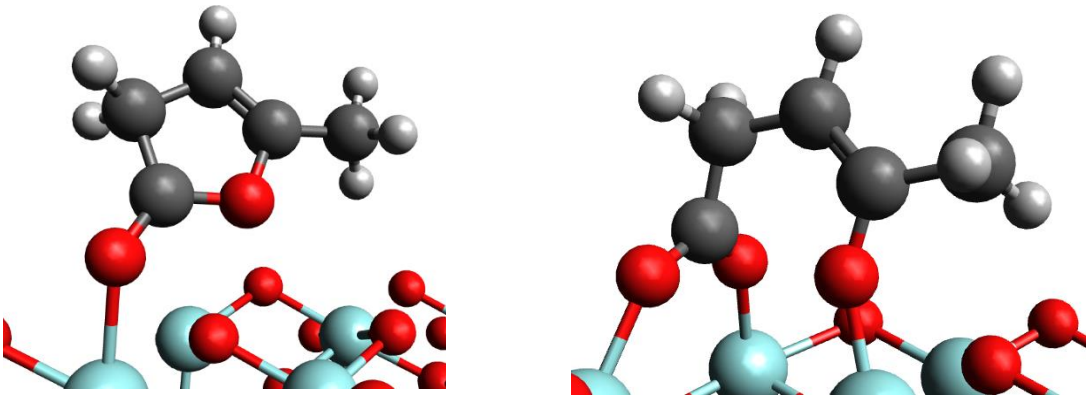

(a) **(b)**

Figure 24 Side view of optimized minimum-energy configurations of αAL on the catalyst surface. The species **(a) αAL**_1 represents the physisorbed closed form, while **(b) αAL_2** depicts the open adsorbed structure (bidentate).

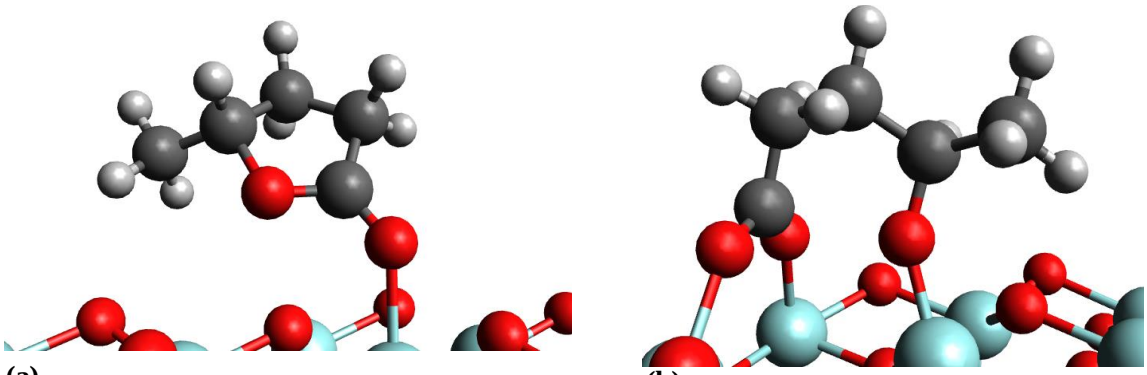

(a) **(b)**

Figure 25 Side view of optimized minimum-energy configurations of GVL on the catalyst surface. The species **(a) GVL_1** represents the physisorbed closed form, while **(b) GVL_2** depicts the open adsorbed structure.

In this thesis, we focus exclusively on the initial step of the CTH reaction, specifically the conversion of ML to αAL, to assess its feasibility. Based on the observed adsorption modes, we proposed a potential reaction mechanism: **Mechanism 1** (**Figure 26**). Initially, the **ML_1** intermediate is formed through physisorption. This intermediate can subsequently transform into the levulinate-like intermediate, **ML_2**. The geometry of **ML_2** indicates a distortion in the ester functional group, with an elongation of the OC-OCH_3 bond, suggesting its susceptibility to cleavage (**Figure 23b**). After an internal proton transfer from α-carbon to the OCH_3 moiety, the release of CH_3OH can occur, leading to the formation of the open form of αAL, designated as **αAL_2**, that has a bidentate structure. Finally, this intermediate may undergo cyclization to form the closed structure, **αAL_1**, that can eventually desorb.

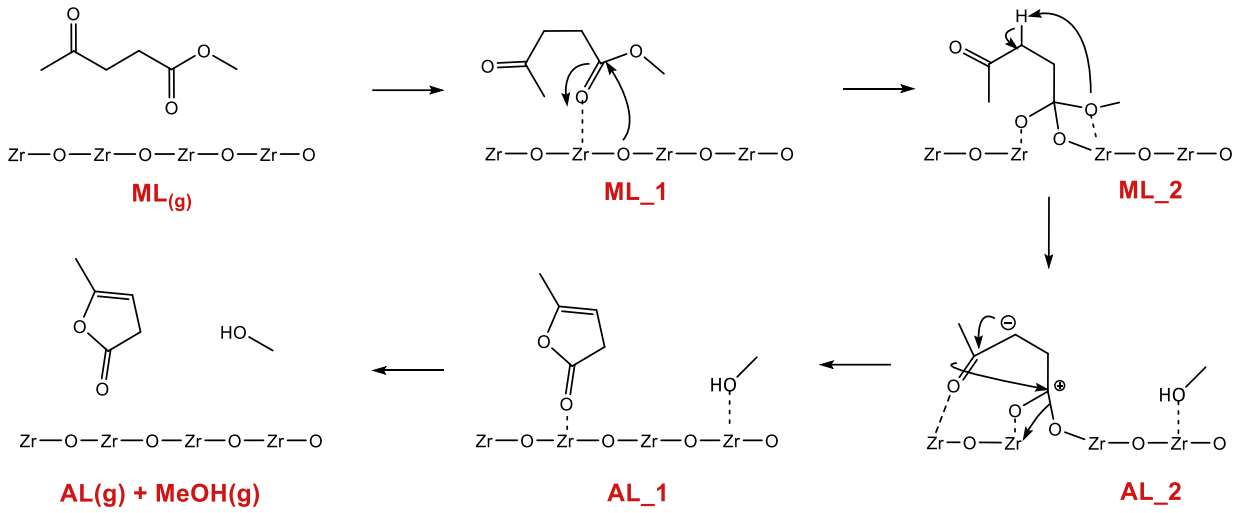

Figure 26 Mechanism 1 for the conversion of ML into αAL

The potential energy surface (**Figure 27**) reveals a significant limitation: while the formation of the open αAL structure (**αAL_2**) is relatively facile from a thermodynamic perspective, the subsequent transformation into the closed form is energetically unfavourable, with a potential energy difference of nearly 2 eV. Such a large energy requirement cannot be met even at the experimental temperature of 250 °C. Moreover, our energy profile does not account for any kinetic barriers, which would further increase the energy cost. This indicates that the transition from **αAL_2** to the closed **αAL_1** form would not occur due to these energy constraints. This suggests that the subsequent CTH reaction may not involve the closed form of αAL, but rather **αAL_2**. However, this hypothesis encounters issues. Specifically, it would imply that the open **αAL_2** must convert to open **GVL_2**. Yet, as mentioned earlier, the closing of GVL would still require at least 1.5 eV. Consequently, we would not be able to detect the formation of GVL in its closed form.

Mechanism 1 appears unlikely, and other hypotheses must be considered. Insights from DRIFT spectra, particularly the detection of hydroxyl groups on the catalyst surface and their depletion after adsorption of ML indicate that these groups may play a key role in the reaction mechanism, opening new avenues for understanding the catalytic process.

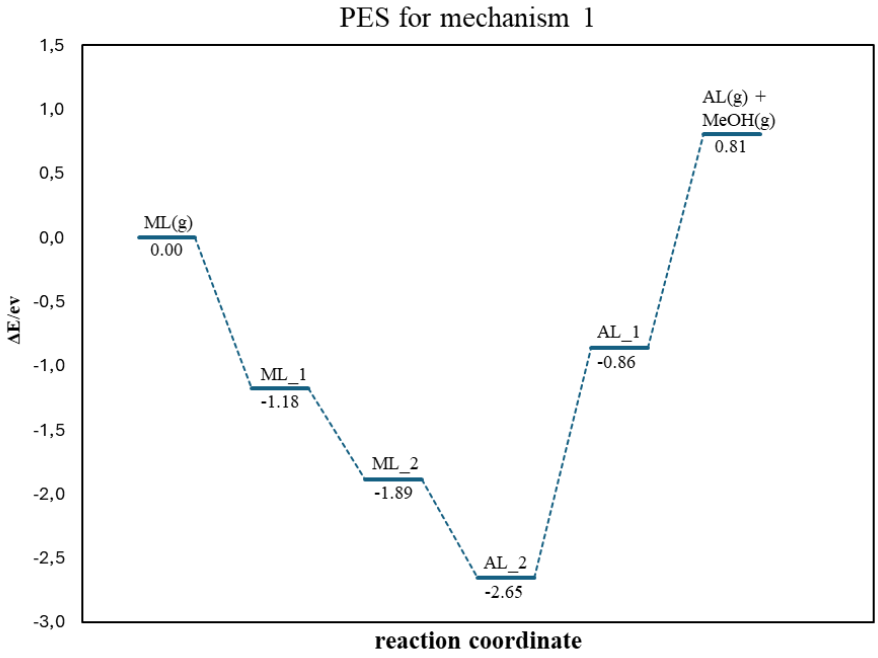

Figure 27 Reaction potential energy surface (PES) for **Mechanism 1**

We propose an alternative mechanistic pathway, referred to as **Mechanism 2** (**Figure 28**), which explicitly involves hydroxyl groups on the catalyst surface. In this pathway, ML initially undergoes physisorption onto the surface, followed by the insertion of a hydroxyl group at the carbonyl carbon. A similar interaction has been proposed in literature for CO_2 on *t*-ZrO_2[67]. This interaction results in the formation of intermediate **i01** (**Figure 29b**), where a significant elongation of the C-OR bond in the ester group is observed (+9.6%). The methoxy group abstracts a nearby proton and is released as methanol, leading to the formation of **levulinate** (**i03**), a bidentate species on the surface (**Figure 30a**).

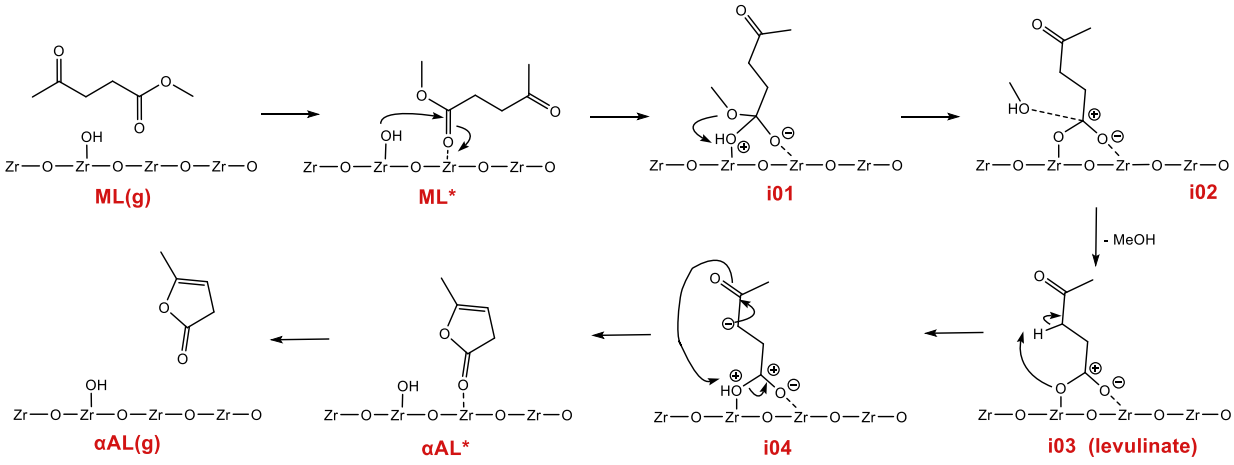

Figure 28 Mechanism 2 for the conversion of ML into αAL.

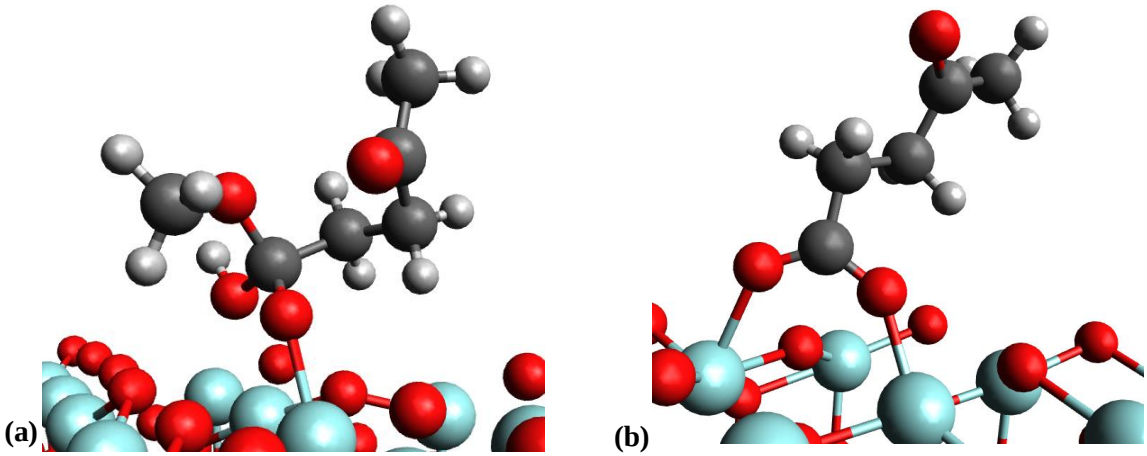

Figure 29 Side view of optimized minimum-energy configurations of ML on the catalyst surface in the presence of a hydroxyl group. The molecule **(a) i01** represents the adsorbed form depicts **(b) i03** the **levulinate** species.

At this stage, a surface-activated oxygen atom abstracts an acidic proton from the α-position relative to the carbonyl, forming **i04** intermediate. The subsequent rearrangement of the negative charge facilitates a nucleophilic attack by the carbonyl carbon, leading to the closure of the ring and the formation of αAL. After the molecule detaches from the surface, the hydroxyl group remains on the catalyst, underscoring its catalytic role in the reaction.

In this alternative mechanism, the potential energy surface (PES) is more favourable, indicating a more plausible and energetically feasible reaction pathway (**Figure 30**). The conversion of the physisorbed ML to **i01** is almost athermic, while the loosing of methanol is slightly endothermic (0.15 eV). Fully desorbing the new formed MeOH requires 0.43 eV. Although kinetic barriers are not considered herein, the formation of the levulinate species, **i03**, appears reasonable from a thermodynamic point of view. Its conversion to **i04** (the open form of αAL), possibly through an intramolecular proton transfer, is the most endergonic step of all the explored PES, requiring 0.46 eV. Once this species is formed, it can be converted into the closed form through a slightly endothermic process (0.16 eV).

The PES of **Mechanism 2** shows that the hydroxyl groups could play some crucial role in modulating the adsorption and reactivity of methyl levulinate, ensuring that the intermediate species are closer in energy and, most importantly, that the ring-closing step is not as energetically demanding as in the previously proposed mechanism. It must be observed that this is only a first investigation, considering only one hydroxyl group on the surface, and more detailed investigations are needed to really rule out the mechanism.

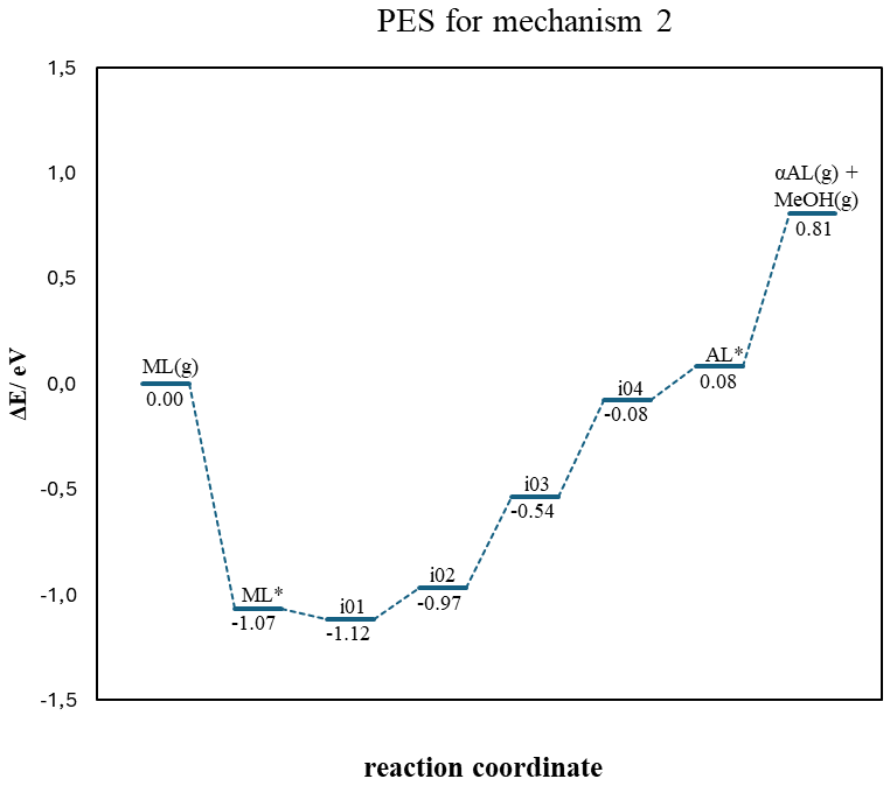

Figure 30 Reaction energy profile of **Mechanism 2.**

In conclusion, two mechanisms have been proposed. Based on the adsorption modes observed for ML on the bare surface, **Mechanism 1** was investigated. In this case the formation of a species strongly interacting through the ester function of ML and an oxygen of the surface, is shown to be thermodynamically favourable. At the same time the formation of the open form of αAL is also favoured, but its closing is highly energy demanding (ΔE = 1.80 eV). Anyway, such kind of mechanism would require a high accessibility of the catalyst surface, and not hydrogenated bridge oxygens. DRIFTS experiments instead showed that hydroxyl groups cover the surface, and their depletion is suggested when adsorbing ML. **Mechanism 1** could be not representative, since apparently OH is involved in the phenomena happening on the surface, but also reduces the accessibility of the surface (and the number of Zr active sites). We proposed **Mechanism 2**, involving an insertion of OH on the ester function of ML. In this case, we only investigated the "local" effect of OH group. We showed that the formation of the levulinate species can be regarded as thermodynamically feasible. The formation of the open form of αAL is now endothermic, but its closure is thermodynamically less demanding than in the case of **Mechanism 1**. Anyway, the kinetic barriers must be included to clearly rule out the feasibility of this mechanism. Overall computations showed that the formation of pseudo-carbonate and

levulinate species on the surface might be straightforward, thanks to the interaction with bridge surface oxygen of hydroxyl group. In both these cases the surface of the catalyst is modified, and the molecule becomes part of the surface. At the same time, the ring closure of αAL is not straightforward to be ruled out.

In the subsequent section, a comprehensive comparison is conducted between the experimental findings and computational predictions, evaluating their level of consistency while addressing the remaining challenges in fully elucidating the catalytic processes involved.

4.4 Comparing Experimental Observations and Computational Predictions

To compare experiments and computational results, we computed the vibrational frequencies of the hypothesized intermediates for **Mechanism 1** and **Mechanism 2** and compared them with the experimental DRIFT spectra. Only the frequencies have been computed, using finite difference method approach (FDM), as implemented in VASP, and intensities are ignored herein. For this reason, the predicted frequencies are represented only as green thick lines in the following figures.

First, we tried to simulate some reference system, in order to test the reliability of the computational protocol. In **Figure 31** and **Figure 32**, the ATR spectra of ML and αAL recorded at 20 °C are compared with the theoretical vibrational frequencies calculated for the isolated molecule. It can be observed that the overlap between the peaks and the calculated vibrational frequencies is generally good, while some discrepancies remain (in particular missing vibrations at wavenumbers where experimental peaks are present). Notably, periodic DFT may not be the most suitable method for simulating a finite system such as a molecule. Furthermore, to be coherent with all the other calculations, PBE functional was employed. Using a localized basis set and a more accurate functional would likely yield more accurate results.

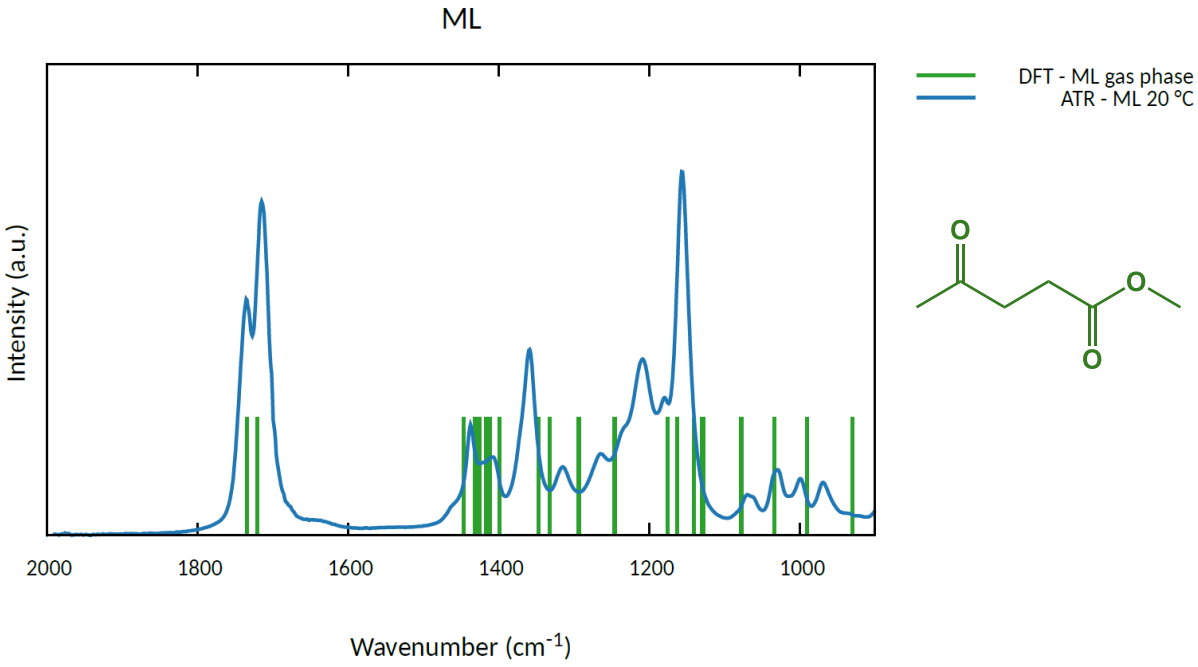

Figure 31 ATR spectrum of ML recorded at 20 °C (**blue line**) and the theoretical vibrational frequencies calculated for the molecule in the gas phase (**green sticks**).

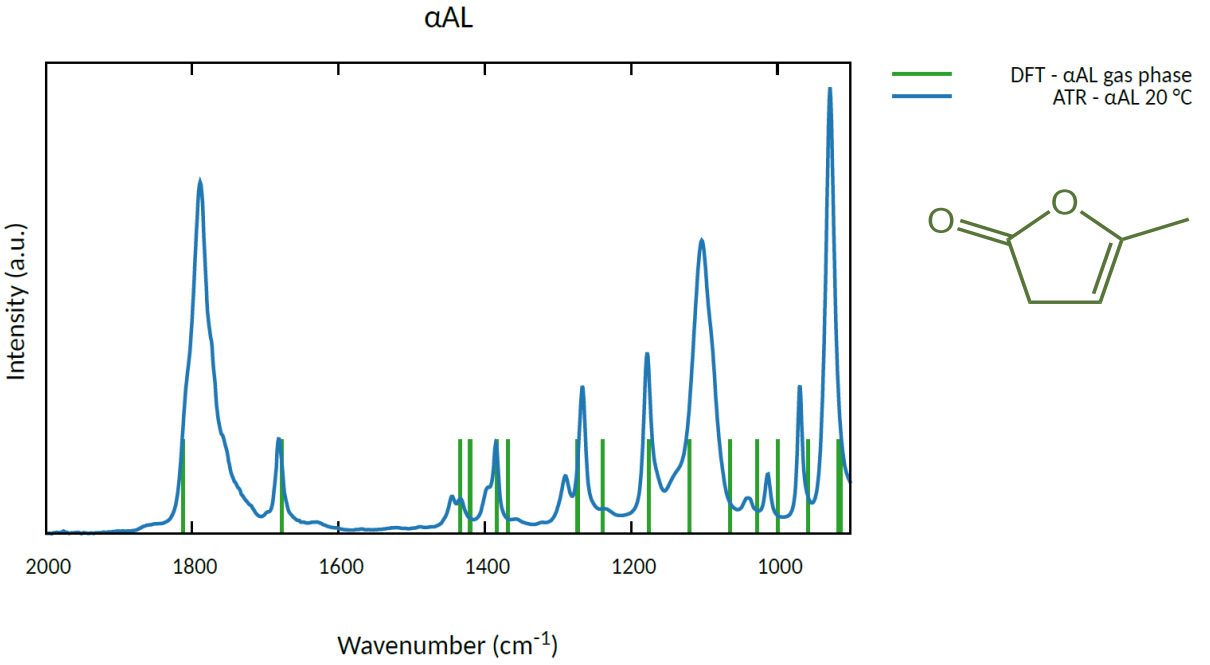

Figure 32 ATR spectrum of αAL recorded at 20 °C (**blue line**) and the theoretical vibrational frequencies calculated for the molecule in the gas phase (**green sticks**).

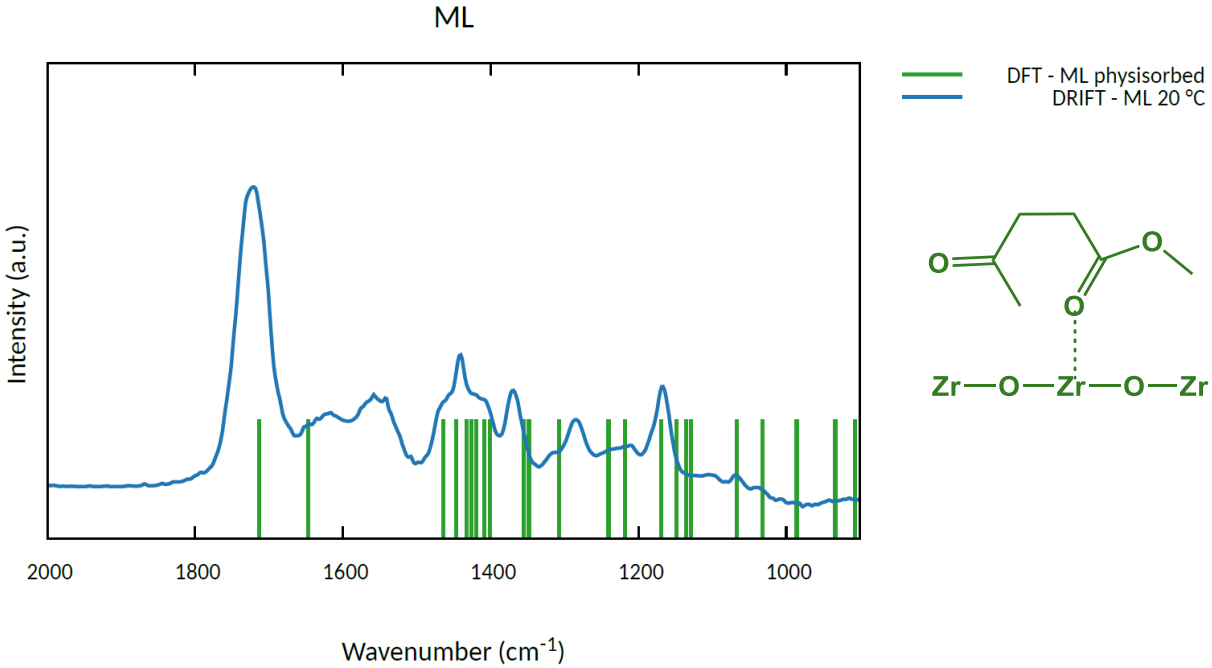

Figure 33 DRIFT spectrum of ML recorded at 20 °C (**blue line**) and the theoretical vibrational frequencies calculated for ML physisorbed on the catalyst surface (**green sticks**).

In **Figure 33**, which compares the DRIFT spectrum of ML recorded at 20 °C with the theoretical vibrational frequencies calculated for the molecule physisorbed on the catalyst surface, the overlap between the peaks and calculated frequencies is precise only in some areas.

We moved to the most interesting DRIFTS spectrum: ML at 250 °C. We proposed that this spectrum, that is superimposable to the one of αAL at the same temperature, can be due to either the ML transformation into βAL or the αAL retro conversion to the levulinate intermediate. **Figure 34** shows the DRIFTS compared with the theoretical vibrational frequencies calculated for both the closed form of βAL and the levulinate adsorbed (**i03**) on the catalyst surface, possibly formed as proposed in **Mechanism 2**. The predicted frequencies for the CO stretching of βAL and the levulinate show almost the same frequencies (1706 and 1712 cm^{-1}). Both the frequencies are well aligned with the experimental peak. While βAL presents a C=C stretching at 1598 cm^{-1} that falls almost in the range of the 1650-1600 cm^{-1} band, it shows no signals around the 1600-1500 cm^{-1} band. At the opposite the levulinate shows no signal in the first area, while it has a frequencies of 1517 cm^{-1}, corresponding to the O-C-O asymmetric stretching, consisting with evidences in literature for similar systems.[55] Both intermediates show frequencies in the area of the band centred at 1445 cm^{-1}. Moving to lower frequencies both systems have computed frequencies in good agreement with the experimental spectrum. This comparison doesn't allow to rule out if levulinate, βAL or both the compounds are present. Anyway, we show that the species responsible for the large band at 1600-1500 cm^{-1} should have a structure like the levulinate. Although the double bond of βAL can explain the band at 1650-1600 cm^{-1}, still we must consider that almost the same band is showed at the same temperature by MV, that is not able to form ALs-like structure.

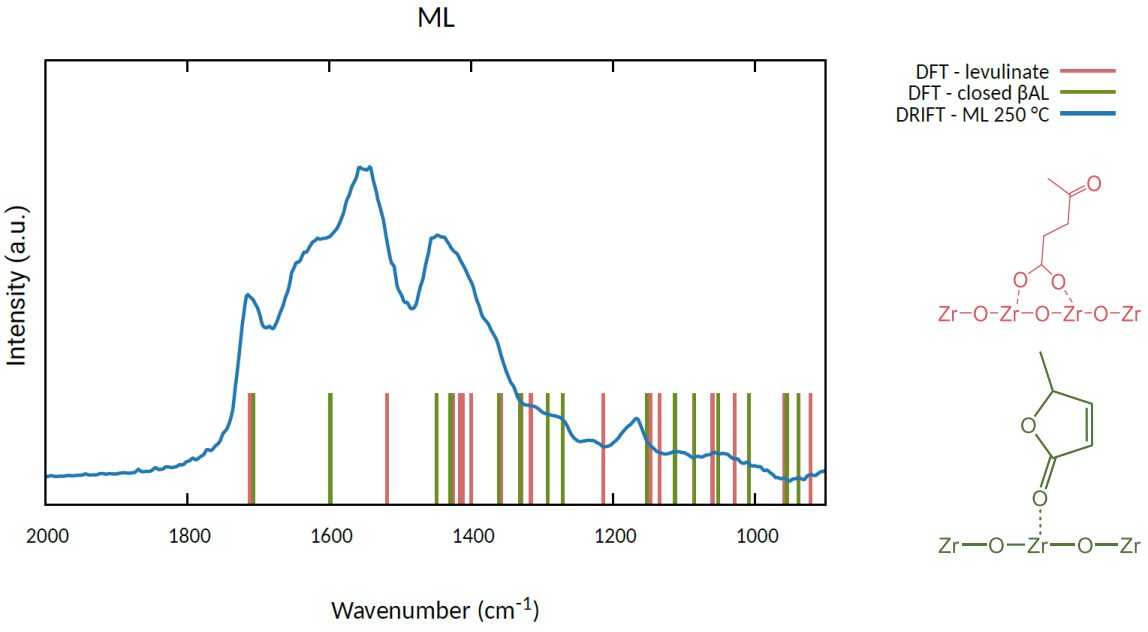

Figure 34 DRIFT spectrum of ML recorded at 250 °C (**blue line**), the theoretical vibrational frequencies calculated for the open adsorbed form of βAL (**green sticks**) and the levulinate (**red sticks**).

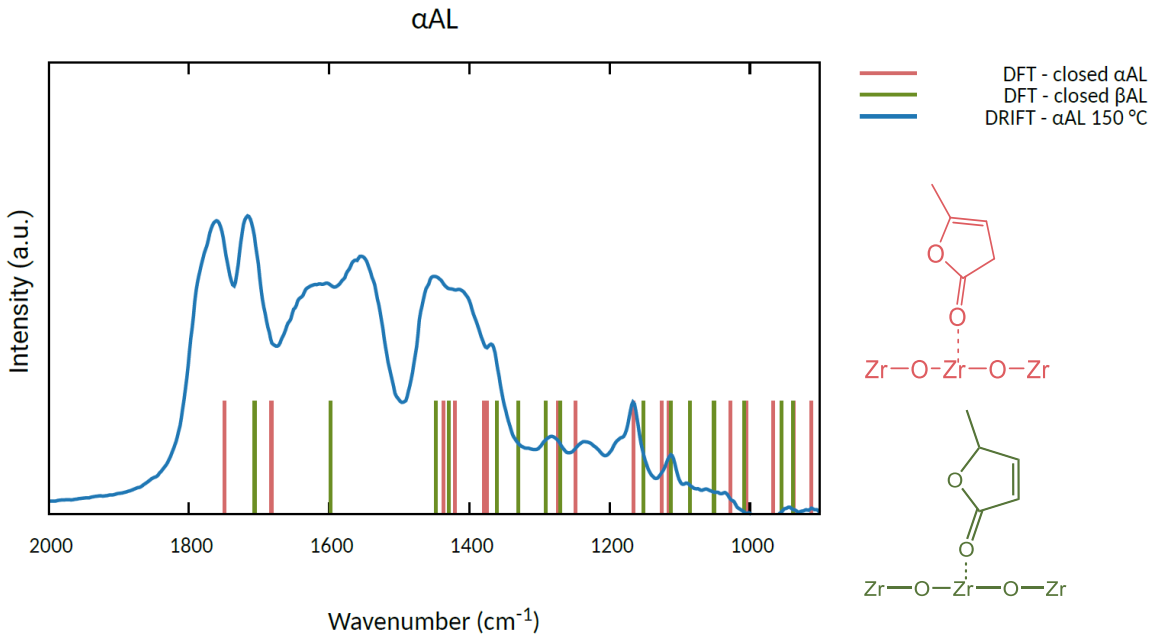

Figure 35 DRIFT spectrum of αAL recorded at 150 °C (**blue line**), the theoretical vibrational frequencies calculated for the closed adsorbed form of βAL (**green sticks**) and the open adsorbed form of βAL (**red sticks**).

Finally, we tried to superimpose the predicted frequencies for αAL and βAL with the DRIFT spectrum of αAL at 150 °C, to verify if the spectrum could be explained assuming a temperature-driven isomerisation (**Figure 35**). From the comparison with the vibrational frequencies of the two isomers of AL, although the CO stretching pulses are slightly shifted relative to the experimental data, the Δν between them, approximately 40 cm^{-1}, corresponds to the difference between the equivalent experimental peaks. Anyway, this would be also true for levulinate and αAL. The two signals for the C=C stretching differs by 83 cm^{-1} and lie at the extremes of the 1650-1600 band. No signals are observed in the 1600-1500 cm^{-1} region.

Overall, the comparison between the experimental spectra and the computed frequencies, provides some useful insights. In fact, we observed that the levulinate species shows a characteristic frequency of 1517 (O-C-O asymmetric stretching) that lie in the 1600-1500 cm^{-1} region, showing that an intermediate with this characteristic could be involved in the reaction. However, we have not been able to rule out if a temperature-driven isomerisation of αAL takes place, or αAL can retro convert to a levulinate-like intermediate. Nonetheless, considering our computed frequencies, a mix of levulinate-like species and ALs on the surface can eventually explain the DRIFT spectrum of ML at 250 °C, and its superimposition with the one of αAL at the same temperature. This would be also consistent with our alternative mechanism, i.e. **Mechanism 2**.

5. Chapter 5 – Conclusions

This thesis combined experimental and computational studies to gain insights into the GVL conversion of methyl levulinate (ML) to GVL using ethanol over *t*-ZrO_2 catalyst. Previous research suggested that this process proceeds via the conversion of ML into ALs, αAL and βAL, which subsequently convert into GVL through ethanol CTH. Therefore, this study focused on the initial step of the reaction: the conversion of ML into ALs.

Through DRIFTS spectroscopy, it was shown that ML is both physisorbed and strongly interacts with the catalyst surface at room temperature, as indicated by bands in the 1650–1500 cm^{-1} range. To clarify the contributions of the ester and ketone groups to this interaction, DRIFTS spectra of 2-P and MV were also recorded. The absence of significant bands in the range of 1650-1500 cm^{-1} for 2-P and their pronounced intensity for MV led to the conclusion that the ester group is primarily responsible for the strong surface interaction. As the temperature increases, the intensity of these bands grows, while the CO stretching band weakens and disappears above 300 °C for ML. These observations align with the high reactivity of the *t*-ZrO_2 (101) surface, as predicted by the computed adsorption modes. When OH groups are absent, ML interacts strongly with the surface (ΔE_{ads} = -1.89 eV) via its ester group, with one surface oxygen interacting with the carbonyl carbon, elongating the C–OR bond. This suggests the ester as the reactive center. According to the proposed **Mechanism 1**, this species can thermodynamically convert into the open form of αAL (ΔE = 0.76 eV), but its cyclization is highly endothermic (ΔE = 1.76 eV). These surface-bound intermediates, while potentially stable and contributing to catalyst poisoning, are unlikely to be the main intermediates in the reaction pathway. In fact, considering just the bare surface might be not a good model, since also the experimental DRIFTS shows that superficial OH groups are present, and they are involved in some phenomena when adsorbing ML and the other investigated esters. Considering the presence of surface OH groups we explored an alternative mechanism, i.e. **Mechanism 2**. Through the insertion of the OH in the ester group of ML, we showed that the formation of a levulinate (bidentate) intermediate can eventually take place. We predicted that such an intermediate is characterized by a predicted vibrational frequency of 1517 cm^{-1} (O-C-O asymmetric stretching). Although we cannot proof that the levulinate is formed, chemical intermediates with this structural characteristic can eventually explain the large band centred at 1545 cm^{-1}, while the nature of the 1650-1600 cm^{-1} band remains unclear. In **Mechanism 2**, the

conversion between the open and closed form of αAL becomes more thermodynamically favorable (ΔE = 0.16 eV) compared to **Mechanism 1**, suggesting that OH groups play a crucial role in catalyzing the reaction and preventing surface poisoning.

Overall, the interaction of ML with the catalyst surface primarily occurs through its ester group, with surficial OH groups playing a pivotal role. This interaction may lead to the formation of levulinate-like intermediates, potentially explaining the spectral bands observed between 1600 and 1500 cm^{-1}, and eventually result in the production of ALs. Notably, at the reaction temperature of 250 °C, the DRIFTS spectra of ML and αAL are nearly identical. In the temperature profile of αAL, a peak emerges at 1716 cm^{-1}, while the one at 1760 cm^{-1} decreases in intensity. Initially, we attributed this feature to the isomerization of αAL to βAL, but this explanation is less likely, as the presence of such esters group at 250 °C on such a reactive surface is improbable (see MV behavior). An alternative explanation is that αAL retroconverts into a levulinate-like intermediate, with the 1716 cm^{-1} band corresponding to the ketone CO stretch, which remains detectable, since the system is grafted to the surface through the ester group and the ketone is far from it and not interacting. Anyway, assuming the presence of a mixture of βAL and levulinate on the surface, our computed frequencies show a good match with the experimental DRIFT spectra recorded at 250 °C for ML. This correspondence suggests that the observed experimental data likely result from the coexistence of multiple phenomena occurring on the catalyst surface.

In conclusion, the combined experimental and computational approaches have proven effective in shedding light on the surface reactivity and the critical role of OH groups in the formation of levulinate and ALs. Although further investigation is required to confirm the formation of ALs and elucidate the structures and roles of levulinate-like intermediates, in the CTH process.

6. Bibliography

1. Demirbas, A. Biofuels securing the planet's future energy needs. *Energy Convers. Manag.* **50**, 2239–2249 (2009).
2. Schaub, T. Efficient Industrial Organic Synthesis and the Principles of Green Chemistry. *Chem. Weinh. Bergstr. Ger.* **27**, 1865–1869 (2021).
3. 12 Principles of Green Chemistry. *American Chemical Society* https://www.acs.org/greenchemistry/principles/12-principles-of-green-chemistry.html.
4. Clark, J. H. *et al.* Green chemistry and the biorefinery: a partnership for a sustainable future. *Green Chem.* **8**, 853–860 (2006).
5. Chemical Routes for the Transformation of Biomass into Chemicals | Chemical Reviews. https://pubs.acs.org/doi/10.1021/cr050989d.
6. Sun, J. X., Sun, X. F., Zhao, H. & Sun, R. C. Isolation and characterization of cellulose from sugarcane bagasse. *Polym. Degrad. Stab.* **84**, 331–339 (2004).
7. General Considerations on Structure and Reactivity of Cellulose: Section 2.1–2.1.4. in *Comprehensive Cellulose Chemistry* 9–29 (John Wiley & Sons, Ltd, 1998). doi:10.1002/3527601929.ch2a.
8. Figure 8. Cellulose strands are surrounded by hemicellulose and lignin... *ResearchGate* https://www.researchgate.net/figure/Cellulose-strands-are-surrounded-by-hemicellulose-and-lignin-in-wood-cell-wall-and-the_fig5_353926717.
9. Leiß, S., Venus, J. & Kamm, B. Fermentative Production of -Lysine–lactate with Fractionated Press Juices from the Green Biorefinery. *Chem. Eng. Technol.* **33**, 2102–2105 (2010).

10. Bozell, J. J. & Petersen, G. R. Technology development for the production of biobased products from biorefinery carbohydrates—the US Department of Energy's "Top 10" revisited. *Green Chem.* **12**, 539–554 (2010).
11. Girisuta, B., Danon, B., Manurung, R., Janssen, L. P. B. M. & Heeres, H. J. Experimental and kinetic modelling studies on the acid-catalysed hydrolysis of the water hyacinth plant to levulinic acid. *Bioresour. Technol.* **99**, 8367–8375 (2008).
12. Hendriks, A. T. W. M. & Zeeman, G. Pretreatments to enhance the digestibility of lignocellulosic biomass. *Bioresour. Technol.* **100**, 10–18 (2009).
13. Bhutto, A. W. *et al.* Insight into progress in pre-treatment of lignocellulosic biomass. *Energy* **122**, 724–745 (2017).
14. Ethanol | Definition, Formula, Uses, & Facts | Britannica. https://www.britannica.com/science/ethanol (2024).
15. Encyclopedia of Analytical Science. *ScienceDirect* http://www.sciencedirect.com:5070/referencework/9780123693976/encyclopedia-of-analytical-science.
16. Vohra, M., Manwar, J., Manmode, R., Padgilwar, S. & Patil, S. Bioethanol production: Feedstock and current technologies. *J. Environ. Chem. Eng.* **2**, 573–584 (2014).
17. Wyman, C. Ethanol Fuel. in *Encyclopedia of Energy* 541–555 (2004). doi:10.1016/B0-12-176480-X/00518-0.
18. Association, R. F. Annual Ethanol Production. *Renewable Fuels Association* https://ethanolrfa.org/markets-and-statistics/annual-ethanol-production.
19. PubChem. Levulinic acid. https://pubchem.ncbi.nlm.nih.gov/compound/11579.
20. Werpy, T. & Petersen, G. *Top Value Added Chemicals from Biomass: Volume I -- Results of Screening for Potential Candidates from Sugars and Synthesis Gas*. DOE/GO-102004-

1992, 15008859 http://www.osti.gov/servlets/purl/15008859/ (2004) doi:10.2172/15008859.

21. Tang, X. *et al.* Production of γ-valerolactone from lignocellulosic biomass for sustainable fuels and chemicals supply. *Renew. Sustain. Energy Rev.* **40**, 608–620 (2014).
22. Chang, C., Ma, X. & Cen, P. Kinetics of Levulinic Acid Formation from Glucose Decomposition at High Temperature1. *Chin. J. Chem. Eng.* **14**, 708–712 (2006).
23. Kuster, B. F. M. 5-Hydroxymethylfurfural (HMF). A Review Focussing on its Manufacture. *Starch - Stärke* **42**, 314–321 (1990).
24. Zhang, J., Wu, S., Li, B. & Zhang, H. Advances in the Catalytic Production of Valuable Levulinic Acid Derivatives. *ChemCatChem* **4**, 1230–1237 (2012).
25. Shrivastav, G., Khan, T. S., Agarwal, M. & Haider, M. A. Reformulation of Gasoline To Replace Aromatics by Biomass-Derived Alkyl Levulinates. *ACS Sustain. Chem. Eng.* **5**, 7118–7127 (2017).
26. Bond, J. Q., Alonso, D. M., Wang, D., West, R. M. & Dumesic, J. A. Integrated Catalytic Conversion of γ-Valerolactone to Liquid Alkenes for Transportation Fuels. *Science* **327**, 1110–1114 (2010).
27. Raj, T. *et al.* Synthesis of γ-valerolactone (GVL) and their applications for lignocellulosic deconstruction for sustainable green biorefineries. *Fuel* **303**, 121333 (2021).
28. Lange, J.-P. *et al.* Valeric biofuels: a platform of cellulosic transportation fuels. *Angew. Chem. Int. Ed Engl.* **49**, 4479–4483 (2010).
29. Gundekari, S. *et al.* Levulinic Acid- and Furan-Based Multifunctional Materials: Opportunities and Challenges. in *Catalysis for Clean Energy and Environmental Sustainability: Biomass Conversion and Green Chemistry - Volume 1* (eds. Pant, K. K., Gupta, S. K. & Ahmad, E.) 291–343 (Springer International Publishing, Cham, 2021). doi:10.1007/978-3-030-65017-9_11.

30. Liguori, F., Moreno-Marrodan, C. & Barbaro, P. Environmentally Friendly Synthesis of γ-Valerolactone by Direct Catalytic Conversion of Renewable Sources. *ACS Catal.* **5**, 1882–1894 (2015).
31. Chen, T. *et al.* Degradable polymers from ring-opening polymerization of α-angelica lactone , a five-membered unsaturated lactone. *Polym. Chem.* **2**, 1190–1194 (2011).
32. Komanoya, T., Nakajima, K., Kitano, M. & Hara, M. Synergistic Catalysis by Lewis Acid and Base Sites on ZrO2 for Meerwein–Ponndorf–Verley Reduction. *J. Phys. Chem. C* **119**, 26540–26546 (2015).
33. Tabanelli, T. *et al.* Transfer Hydrogenation of Methyl and Ethyl Levulinate Promoted by a ZrO2 Catalyst: Comparison of Batch vs Continuous Gas-Flow Conditions. *ACS Sustain. Chem. Eng.* **7**, 9937–9947 (2019).
34. Schlexer Lamoureux, P. *et al.* Machine Learning for Computational Heterogeneous Catalysis. *ChemCatChem* **11**, 3581–3601 (2019).
35. Réocreux, R. & Michel, C. Rational design of heterogeneous catalysts for biomass conversion – Inputs from computational chemistry. *Curr. Opin. Green Sustain. Chem.* **10**, 51–59 (2018).
36. Ruppert, A. M. *et al.* Ru catalysts for levulinic acid hydrogenation with formic acid as a hydrogen source. *Green Chem.* **18**, 2014–2028 (2016).
37. Siddiqui, N. *et al.* Study of γ-valerolactone production from hydrogenation of levulinic acid over nanostructured Pt-hydrotalcite catalysts at low temperature. *Fuel* **323**, 124272 (2022).
38. Vásquez, P. B. *et al.* Gas-Phase Catalytic Transfer Hydrogenation of Methyl Levulinate with Ethanol over ZrO2. *ACS Sustain. Chem. Eng.* **7**, 8317–8330 (2019).
39. Bacchiocchi, R. *et al.* Structure-activity relationships of ZrO2 crystalline phases in the catalytic transfer hydrogenation of methyl levulinate with ethanol. *J. Catal.* **428**, 115177 (2023).

40. The Definition of the Model. in *A Chemist's Guide to Density Functional Theory* 1–1 (John Wiley & Sons, Ltd, 2001). doi:10.1002/3527600043.part1.
41. The Hohenberg-Kohn Theorems. in *A Chemist's Guide to Density Functional Theory* 33–40 (John Wiley & Sons, Ltd, 2001). doi:10.1002/3527600043.ch4.
42. The Kohn-Sham Approach. in *A Chemist's Guide to Density Functional Theory* 41–64 (John Wiley & Sons, Ltd, 2001). doi:10.1002/3527600043.ch5.
43. Dudarev, S. L., Botton, G. A., Savrasov, S. Y., Humphreys, C. J. & Sutton, A. P. Electron-energy-loss spectra and the structural stability of nickel oxide: An LSDA+U study. *Phys. Rev. B* **57**, 1505–1509 (1998).
44. Himmetoglu, B., Floris, A., de Gironcoli, S. & Cococcioni, M. Hubbard-corrected DFT energy functionals: the LDA+U description of correlated systems. *arXiv.org* https://arxiv.org/abs/1309.3355v1 (2013) doi:10.1002/qua.24521.
45. The VASP Manual - VASP Wiki. https://www.vasp.at/wiki/index.php/The_VASP_Manual.
46. Quantum-chemical Approaches: Section 2.1 - 2.10. in *Computational Chemistry of Solid State Materials* 45–105 (John Wiley & Sons, Ltd, 2005). doi:10.1002/9783527612277.ch2a.
47. #19 Pseudopotential for Efficient Simulation. *Materials Square* http://www.materialssquare.com/blog/19-pseudopotential-for-efficient-simulation.
48. Blöchl, P. E. Projector augmented-wave method. *Phys. Rev. B* **50**, 17953–17979 (1994).
49. Kresse, G. & Joubert, D. From ultrasoft pseudopotentials to the projector augmented-wave method. *Phys. Rev. B* **59**, 1758–1775 (1999).
50. Chen, B. W. J., Xu, L. & Mavrikakis, M. Computational Methods in Heterogeneous Catalysis. *Chem. Rev.* **121**, 1007–1048 (2021).

51. Armaroli, T., Bécue, T. & Gautier, S. Diffuse Reflection Infrared Spectroscopy (Drifts): Application to the in Situ Analysis of Catalysts. *Oil Gas Sci. Technol.* **59**, 215–237 (2004).
52. Arregoitia-Quezada, M. *et al.* Effect of the method and impregnation time on the surface acidity of zirconia modified with boron. *J. Sol-Gel Sci. Technol.* **82**, (2017).
53. Launer, P. & Arkles, B. Infrared Analysis of Organsilicon Compounds: Spectra-Structure Correlations. in *Reprinted from Silicone Compounds Register and Review* 223–226 (2008).
54. Moraes, T. S. *et al.* Ethanol conversion at low temperature over CeO2—Supported Ni-based catalysts. Effect of Pt addition to Ni catalyst. *Appl. Catal. B Environ.* **181**, 754–768 (2016).
55. Hill, I. M., Hanspal, S., Young, Z. D. & Davis, R. J. DRIFTS of Probe Molecules Adsorbed on Magnesia, Zirconia, and Hydroxyapatite Catalysts. *J. Phys. Chem. C* **119**, 9186–9197 (2015).
56. Rintramee, K., Föttinger, K., Rupprechter, G. & Wittayakun, J. Ethanol adsorption and oxidation on bimetallic catalysts containing platinum and base metal oxide supported on MCM-41. *Appl. Catal. B Environ.* **115–116**, 225–235 (2012).
57. de Lima, S. M. *et al.* H2 production through steam reforming of ethanol over Pt/ZrO2, Pt/CeO2 and Pt/CeZrO2 catalysts. *Catal. Today* **138**, 162–168 (2008).
58. Mattos, L. V. & Noronha, F. B. Hydrogen production for fuel cell applications by ethanol partial oxidation on Pt/CeO2 catalysts: the effect of the reaction conditions and reaction mechanism. *J. Catal.* **233**, 453–463 (2005).
59. Panchenko, V. N., Zaytseva, Yu. A., Simonov, M. N., Simakova, I. L. & Paukshtis, E. A. DRIFTS and UV–vis DRS study of valeric acid ketonization mechanism over ZrO2 in hydrogen atmosphere. *J. Mol. Catal. Chem.* **388–389**, 133–140 (2014).

60. Tosoni, S., Chen, H.-Y. T. & Pacchioni, G. A DFT Study of the Reactivity of Anatase TiO2 and Tetragonal ZrO2 Stepped Surfaces Compared to the Regular (101) Terraces. *ChemPhysChem* **16**, 3642–3651 (2015).
61. Xu, X. *et al.* Insights into CO2 methanation mechanism on cubic ZrO2 supported Ni catalyst via a combination of experiments and DFT calculations. *Fuel* **283**, 118867 (2021).
62. Materials Project. https://legacy.materialsproject.org/.
63. Piskorz, W. *et al.* Periodic DFT Study of the Tetragonal ZrO2 Nanocrystals: Equilibrium Morphology Modeling and Atomistic Surface Hydration Thermodynamics. *J. Phys. Chem. C* **116**, 19307–19320 (2012).
64. Arce-Ramos, J.-M., Grabow, L. C., Handy, B. E. & Cárdenas-Galindo, M.-G. Nature of Acid Sites in Silica-Supported Zirconium Oxide: A Combined Experimental and Periodic DFT Study. *J. Phys. Chem. C* **119**, 15150–15159 (2015).
65. Chen, H.-Y. T., Tosoni, S. & Pacchioni, G. A DFT study of the acid–base properties of anatase TiO2 and tetragonal ZrO2 by adsorption of CO and CO2 probe molecules. *Surf. Sci.* **652**, 163–171 (2016).
66. Rittiruam, M. *et al.* Experimental and DFT investigations of the performance of ZrO2 catalysts modified with Ce, La, Y, Mg, and Ba oxides during methyl stearate ketonization. *Appl. Surf. Sci.* **585**, 152627 (2022).
67. Köck, E.-M., Kogler, M., Bielz, T., Klötzer, B. & Penner, S. In Situ FT-IR Spectroscopic Study of CO2 and CO Adsorption on Y2O3, ZrO2, and Yttria-Stabilized ZrO2. *J. Phys. Chem. C* **117**, 17666–17673 (2013).